

Orbital magnetic states in moiré graphene systems

Jianpeng Liu  and Xi Dai 

Abstract | Moiré graphene systems have attracted considerable attention in the past 3 years because they exhibit exotic phenomena including correlated insulating states, unconventional superconductivity and the quantum anomalous Hall effect. All these phenomena are intimately related to the valley-spin-degenerate and topologically non-trivial flat bands in moiré graphene systems. When time-reversal symmetry is broken spontaneously, such flavour-degenerate topological flat bands exhibit unconventional orbital magnetism associated with real-space current-loop patterns on the moiré length scale. In this Perspective, we first survey key experimental progress on the correlated insulating states and the quantum anomalous Hall phenomena. Most of these phenomena are related to the moiré orbital magnetic states, which originate from the topological nature of the moiré flat bands. Finally, we discuss theoretical progress in the understanding of the correlated insulating and quantum anomalous Hall phenomena from the perspective of spontaneous symmetry breaking.

Magnetization in materials has two known origins: the intrinsic spin degrees of freedom and the orbital motions of electrons. For most magnetic materials, both sources contribute to the spontaneous magnetic order, and correspond to the spin and orbital moments, respectively. Unlike the intrinsic spin moment, the orbital moment is caused by electric current loops at the atomic scale below about 1 nm, which are usually generated by the spin–orbit coupling (SOC) and thus considered to be a secondary effect. In principle, these atomic and/or molecular orbital magnetic moments can also be spontaneously aligned or ordered in some pattern by themselves without SOC, leading to a pure ‘orbital magnetic state’. Such an atomic-scale orbital magnetic state has been theoretically discussed in high- T_c cuprates as ‘spontaneous loop current states’¹, but no convincing experimental evidence has yet been observed.

A trivial example of the orbital magnetic system is a free 2D electron gas subject to strong external magnetic fields. The kinetic energy of the electrons is quenched because they are forced to perform cyclotron motions by the external magnetic fields,

and the corresponding energy levels are flat Landau levels (LLs). The cyclotron motion of electrons gives rise to chiral charge current loops, which generate orbital magnetic moments. Two key concepts in modern condensed matter physics — topology and strong Coulomb correlations — are linked up in the physics of LLs leading to many exotic phenomena². If the chemical potential is in the gap between two Landau levels, electrons drift transversely in response to a longitudinal electric field, with quantized Hall conductivity in units of e^2/h (REF.³), which is topologically protected by the topological invariants carried by the occupied LLs⁴. Moreover, because the LLs are perfectly flat, the Coulomb interactions would completely dominate over the kinetic energy, leading to a number of exotic phenomena including the fractional quantum Hall effect^{5,6} and the spontaneous symmetry breaking of LLs with degenerate intrinsic degrees of freedom (such as spin, valley and layer)².

Motivated by the intriguing physics of LLs, theorists have made proposals to realize topologically non-trivial flat bands in artificial lattice models^{7–9}, which have not

yet been realized in experiments. However, in 2011 it was theoretically proposed that flat bands can also exist in an engineered system in which two graphene monolayers are twisted with respect to each other by an angle θ (REF.¹⁰). A moiré supercell is formed in real space as a result of the twist, which greatly changes the electronic structure of the system^{11–15}. It was shown theoretically that at a set of small ‘magic angles’, flat bands with vanishing Fermi velocities emerge from the large moiré supercell of such twisted bilayer graphene (TBG)¹⁰. This fascinating proposal was realized in experiments in March 2018^{16,17}. Experimentalists were able to tune the TBG system to the first magic angle $\theta \approx 1.1^\circ$ and to observe the emergence of correlated insulating states when the flat bands were half filled¹⁷. Surprisingly, superconductivity appears when the filling slightly deviates from $\pm 1/2$ (REF.¹⁶) around the magic angle $\sim 1.05^\circ$. Moreover, the angle around which superconductivity shows up can be further increased by compressing the two graphene layers¹⁸. Such discoveries make the TBG system a useful one in which to study various exotic physics caused by correlation effects among the Dirac electrons.

A few months later, several theoretical groups found that the flat bands in TBG also exhibit non-trivial ‘fragile’ topological properties characterized by the non-trivial winding of ‘Wilson loops’^{19–21}. It was further shown that, without the intra-sublattice component of the moiré potential, the eight flat bands of magic-angle TBG (including the valley and spin degrees of freedom) can be interpreted as originating from eight zeroth pseudo-LLs of Dirac fermions²², a result which provides an intuitive physical picture of the origin of the non-trivial band topology in TBG. Analytical wavefunctions of the flat bands in the ‘chiral limit’ (in which the intra-sublattice moiré potential is set to zero) are highly reminiscent of the lowest LL wavefunctions on a torus²³. These theoretical results make connections between the correlation effects in magic-angle TBG to quantum Hall ferromagnetism. In particular, if an integer number of the eight valley-spin-degenerate topological flat bands are occupied, then the occupied flat bands may be split from the unoccupied ones, owing to the

exchange part of the long-range Coulomb interactions. This splitting opens a gap between the moiré sub-bands with possible non-zero Chern numbers, which carries net orbital magnetizations at the scale of the moiré supercell. Indeed, such orbital magnetic states with (quantum) anomalous Hall effect (AHE) have been observed in TBG aligned with a hexagonal boron nitride (hBN) substrate at 3/4 filling with Chern number ± 1 (REFS^{24,25}), and at $-1/2$ filling with Chern number ± 2 (REF.²⁶).

Topological flat bands with non-zero valley Chern numbers also exist in twisted multilayer graphene systems^{27–34} and in trilayer graphene aligned with an hBN substrate^{35,36}. In particular, evidence for spin-polarized correlated insulating states has been observed at $1/2$ filling of the flat bands in twisted double bilayer graphene (TDBG). The quantum anomalous Hall (QAH) effect with Chern number 2 has already been observed at $-1/4$ filling of the flat bands in hBN-aligned trilayer graphene³⁷, and in twisted bilayer–monolayer graphene system at $1/4$ and $3/4$ fillings³⁸. These observations indicate that the orbital ferromagnetic states with non-zero Chern numbers may generically exist in twisted graphene and moiré graphene systems at partial fillings of the topological flat bands.

Recent scanning tunnelling microscopy (STM) and compressibility measurements indicate a cascade of phase transitions, each occurring at an integer filling of TBG around the magic angle^{39,40}. At each integer filling, the system tends to lift the flavour (valley/spin/sublattice) degeneracy either by flavour polarization⁴¹ or by inter-flavour coupling^{42–44}, implying that the ground states at partial integer fillings may be spontaneous-symmetry-breaking insulating or semi-metallic states. Moreover, by virtue of the non-trivial topological properties of the flat bands, a spontaneous-symmetry-breaking state in the twisted graphene system can exhibit various real-space current-loop patterns^{28,41,44}, which lead to different types of orbital magnetism. For example, in a TBG system without the alignment of an hBN substrate, a valley-polarized state exhibits opposite circulating current-loop patterns on the moiré length scale, leading to a moiré orbital antiferromagnetic state⁴¹. Another example is a ‘Kramers intervalley-coherent state’, which is proposed⁴⁴ as the ground state at the charge-neutrality point and $\pm 1/2$ fillings and exhibits compensating current loops with staggered orbital magnetic fluxes on the atomic length scale.

The alignment of the hBN substrate with graphene would impose a staggered sublattice potential, which breaks C_{2z} symmetry. This potential is crucial in achieving non-zero valley Chern numbers in TBG^{22,25,45,46}. As a result, valley-polarized states in hBN-aligned TBG are typically moiré orbital ferromagnetic states with non-zero Chern numbers at different partial integer fillings, as indicated by recent transport measurements at $3/4$ fillings^{24,25}. These ideas can be straightforwardly generalized to twisted graphene multilayers and trilayer graphene aligned with an hBN substrate^{27,28,30,34–38}. The breaking of C_{2z} symmetry in these systems allows for non-zero valley Chern numbers, which would give rise to moiré orbital ferromagnetic states once the valley symmetry is broken by Coulomb interactions. It is worthwhile to note that, although such a simplified picture is helpful in understanding the QAH phenomena, it cannot explain the elusive correlated insulator states^{17,47,48} and the complicated single-particle excitation spectra^{39,49–52} observed in TBG. The latter requires careful numerical treatments of the full Hamiltonian including both the non-negligible kinetic-energy term and the Coulomb-interaction term, which is discussed in detail later in this Perspective.

In this Perspective, we focus on the the orbital magnetism and QAH effect in twisted graphene systems. We review the electronic structures and topological properties of TBG, twisted multilayer graphene and hBN–graphene systems. We show that topologically non-trivial flat bands are ubiquitous in moiré graphene systems, and are associated with unique orbital magnetism and current-loop patterns in the moiré superlattices. More interestingly, previous theoretical studies indicate that there are in fact multiple competing orders existing at different integer fillings of the flat bands in TBG. Some of these proposed ground states break time-reversal symmetry and are associated with current-loop patterns either on the moiré length scale^{28,41} or on the atomic length scale⁴⁴.

Moiré lattice structures and symmetries

We start our discussion by introducing the moiré superlattice structures in twisted graphene systems. Moiré patterns with long periods can be formed when two ‘slightly different’ atomic layers are placed together. The slight difference can be a mismatch between the lattice constants or a mutual twist by an angle θ . Given a lattice vector \mathbf{R}_1 in the bottom layer, if the corresponding

lattice vector of the top layer \mathbf{R}_2 is expanded or compressed by a factor of η and twisted counterclockwise by an angle θ , then $\mathbf{R}_2 = \eta \mathcal{R}(\theta) \mathbf{R}_1$, where $\mathcal{R}(\theta)$ is the rotation matrix in Cartesian coordinates. When the mismatch of the two lattice vectors is commensurate with one of the primitive lattice vectors \mathbf{a} , that is, $\eta \mathcal{R}(\theta) \mathbf{R}_1 - \mathbf{R}_1 = \mathbf{a}$, the system forms a periodic moiré pattern in real space with the moiré superlattice constant $L_s = a / \sqrt{\eta^2 + 1 - 2\eta \cos \theta}$. Clearly L_s would be much greater than the original lattice constant a when $\eta \approx 1$ and θ is small. For TBG, $\eta = 1$; it follows that $L_s = a / (2 \sin(\theta/2))$, where $a = 2.46 \text{ \AA}$ is the graphene lattice constant. The moiré pattern of TBG is schematically shown in FIG. 1a. There are periodic modulations of the AA and AB/BA regions in which the system is locally stacked as AA bilayer graphene (the two layers are perfectly aligned) and AB/BA (half the atoms of one layer lie over atoms of the other layer and half lie between the atoms of the other layer). As the moiré period $L_s \gg a$, the corresponding moiré Brillouin zone (BZ) is much smaller than the atomic BZ of graphene (FIG. 1b). The moiré BZ only covers a small part of the atomic BZ near the K and K' valleys of graphene. Moreover, after the twist, the K (K') points of the two monolayers K_1 (K') and K_2 (K') are mapped to the K_s and K'_s points of the moiré supercell BZ (FIG. 1b). It is important to note that TBG has atomic corrugations, that is, the interlayer distance varies spatially⁵³. In the AB/BA region the interlayer distance $d_{AB} \approx 3.35 \text{ \AA}$, whereas the interlayer distance $d_{AA} \approx 3.6 \text{ \AA}$ (REF.⁵⁴) in the AA-stacked region. The atomic corrugations have important effects in the low-energy electronic structures of TBG, as discussed in the section on topology.

Other moiré graphene systems include: twisted multilayer graphene systems in which an M -layer graphene and N -layer graphene are stacked together and twisted with respect to each other by an angle θ (FIG. 1c,d); graphene monolayer or multilayers aligned with other 2D materials with similar lattice constants such as hBN (FIG. 1e); and graphene multilayers with multiple twists^{55,56}, alternating twists^{57,58} or even continuously twisted infinite graphene systems⁵⁹. Typical examples for twisted multilayer graphene system include TDBG ($M=N=2$; FIG. 1c) and twisted bilayer+monolayer ($M=2, N=1$; FIG. 1d) systems. The former consists of two AB/BA-stacked graphene bilayers twisted with respect to each other by an angle θ , and the latter is made of a graphene monolayer stacked on top of an AB/BA-stacked bilayer with a twist angle θ . In hBN–graphene

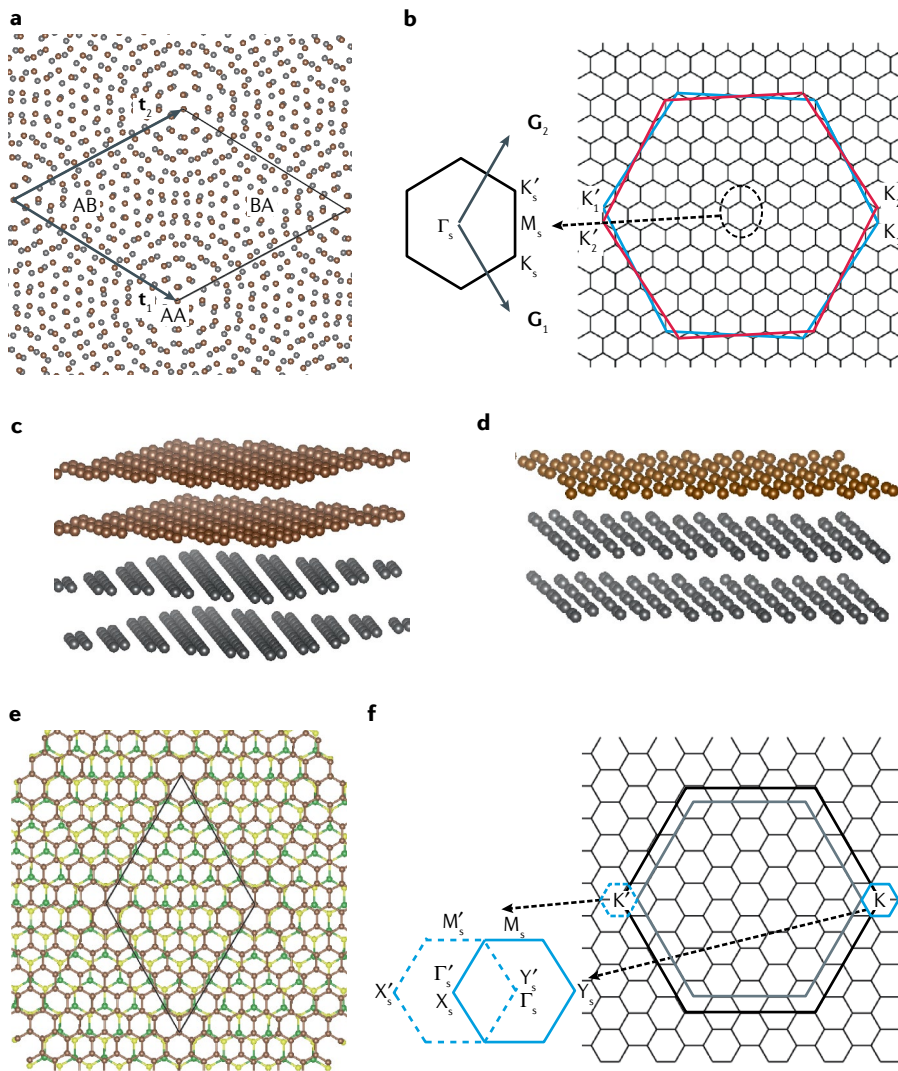


Fig. 1 | Moiré graphene systems. **a** | The lattice structure of twisted bilayer graphene (TBG), with lattice vectors \mathbf{t}_1 and \mathbf{t}_2 . **b** | The moiré Brillouin zone for twisted graphene systems. **c** | Twisted double bilayer graphene. **d** | Twisted bilayer-monolayer graphene. **e** | The moiré superlattice of graphene on a hexagonal boron nitride (hBN) substrate. **f** | Moiré Brillouin zone for hBN-graphene systems. \mathbf{G}_1 , \mathbf{G}_2 , moiré reciprocal lattice vectors of TBG; Γ_s , Γ'_s , K_s , K'_s , M_s , M'_s , X_s , X'_s , Y_s , Y'_s , high-symmetry points in the moiré Brillouin zone of TBG and hBN-graphene.

multilayer heterostructures, the moiré pattern is formed due to the slight mismatch between the lattice constants (FIG. 1e). The moiré BZ for TDBG and other twisted multilayers is the same as that of TBG. In contrast, the moiré pattern in hBN-aligned graphene multilayers (FIG. 1f) results from the mismatch of lattice constants. As a result, the moiré BZ of hBN-graphene system is rotated by 90° compared with that of TBG, and the centres of the moiré BZ for the K and K' valleys (Γ_s and Γ'_s) are shifted with respect to each other by $4\pi/(3L_s)$ as shown in FIG. 1f.

In this Perspective, we focus on situations in which there is a single moiré pattern in the system, but it is also possible to form a 'moiré of moiré superlattice' by placing

multiple moiré patterns together. The system forms a commensurate supercell structure only when the two moiré patterns become commensurate. A typical example of such a system is continuously twisted trilayer graphene in which the first and second layers are twisted with respect to each other by θ_1 , and the second and third layers are twisted by θ_2 . Such a system has been proposed as a 'perfect metal' that has all bands connected to each other⁵⁵, in which correlated insulating and superconducting states have also been observed⁶⁰. Continuously twisted 3D systems, such as a continuously twisted bulk graphite system in which every two adjacent graphene layers are twisted with respect to each other by angle θ (REF.⁵⁹), are predicted to host 3D bulk Weyl nodes.

It is worth noting that when TBG is aligned with an hBN substrate, there are also two moiré patterns: one from the mutual twist of the two graphene layers, and the other from the lattice mismatch between the hBN and the graphene layers. However, the moiré potential from the hBN substrate is an order of magnitude weaker than that from the mutual twist^{61,62}. Therefore the effect of the hBN moiré can be neglected in hBN-aligned TBG systems, and the leading-order effect of the hBN substrate is to impose a staggered sublattice potential on the bottom layer of graphene, which breaks C_{2z} (sublattice) symmetry.

The electronic structures of moiré graphene systems with large moiré periods can be well described by the continuum model of TBG^{10,14,63}. This model has been generalized to hBN-aligned graphene systems^{61,62} and twisted multilayer graphene systems^{27–34}. The low-energy electronic structures of all the moiré graphene systems can be interpreted as follows. First, owing to the formation of the moiré supercell, the low-energy states around the K and K' valleys from the graphene monolayers or multilayers are folded into the moiré supercell BZ, leading to strongly entangled bands. Because the moiré BZ is small at small twist angles, the characteristic bandwidth w_s of these folded graphene bands is also small: $w_s \sim \theta^N$ if the untwisted low-energy band structure $E(\mathbf{k}) \sim k^N$, where N is a positive integer. Second, the states folded into the moiré BZ are further coupled with the moiré potential (denoted by $U(\mathbf{r})$) generated by the moiré pattern. This coupling opens gaps between the entangled bands, giving rise to isolated moiré bands with small bandwidth and typically with non-trivial topological properties. In TBG, the characteristic moiré bandwidth $w_s \pi \hbar v_F / L_s \sim 2 \pi \hbar v_F \sin(\theta/2) / a$, where the bulk Fermi velocity $\hbar v_F \approx 5.25 \text{ eV } \text{\AA}$, and the interlayer moiré potential $U(\mathbf{r}) \approx 0.1 \text{ eV}$ (REFS^{10,14}). The latter is (approximately) independent of θ for small θ when a continuum description of the moiré system applies.

The effect of the twist can be divided into regimes that depend on the twist angle θ . For $\theta \gtrsim 5^\circ$, the effects of interlayer moiré potential opens up small gaps in the folded Dirac bands near the moiré BZ boundary; these gaps have been directly observed by angle-resolved photoemission spectroscopy (ARPES)⁶⁴. For small twist angles $\theta \lesssim 3^\circ$, the effects of $U(\mathbf{r})$ on the folded Dirac cones are no longer perturbative. In this case, two low-energy Dirac bands (per spin valley) with renormalized Dirac Fermi

velocities⁶⁵ would be energetically separated from the remote energy bands. There are two van Hove singularities contributed by the two low-energy bands, which merge toward each other if the twist angle is decreased⁶⁶. The energy separation of the two van Hove peaks is also strongly renormalized by the interlayer moiré potential⁶⁷. If $\theta \lesssim 1.5^\circ$, the interlayer moiré potential is comparable to w_s , and flat bands with exactly vanishing Fermi velocities appear at a set of magic angles¹⁰; the first magic angle is approximately 1.05° . Around the first magic angle, the moiré band structure is strongly renormalized by the moiré potential such that the bandwidth is significantly reduced (≈ 10 meV). In this case, the characteristic Coulomb repulsion energy $V_C \sim e^2/(4\pi\epsilon L_s) \approx 25$ meV (assuming a background dielectric constant of about 4) would dominate over the kinetic energy, and various correlated states show up. In this Perspective, we focus on the magic-angle regime. Although such exact magic angles do not exist in twisted multilayer graphene and hBN-aligned graphene systems, isolated flat bands with small bandwidths of about 10 meV are still present in those systems, and are highly tunable by vertical displacement fields.

Graphene has two valleys K and K', and the states around either K or K' valleys can be separately folded into the moiré BZ, leading to the time-reversal-protected valley degeneracy. Moreover, for small twist angles the separation between the low-energy states around the K and K' valleys $\sim |\mathbf{K} - \mathbf{K}'| = 4\pi/(3a)$ is much greater than the size of the moiré reciprocal lattice vector $|\mathbf{g}_1| = 4\pi/(\sqrt{3}L_s)$. As a result, the coupling between the low-energy states around the two valleys can be neglected, because the Fourier components of the corresponding moiré potential $U(|\mathbf{K} - \mathbf{K}'|)$ are vanishingly small given that the potential $U(\mathbf{r})$ is smooth on the moiré length scale and that $L_s \gg a$. Because the low-energy states of TBG from the two valleys are decoupled from each other, the charge is separately conserved for each valley, and the low-energy subspace of the system has an emergent valley U(1) symmetry⁴² (dubbed $U_v(1)$). Moreover, because spin-orbit coupling is negligible in graphene and at the non-interacting level the two valleys are approximately decoupled for small twist angles, to the leading-order approximation there is a separate spin SU(2) symmetry for each valley. Therefore, all moiré graphene systems have the approximate continuous $U(1) \times U_v(1) \times SU(2) \times SU(2)$ symmetry⁴², where U(1) represents global charge

conservation symmetry. The separate spin rotational symmetry for each valley can be broken by intervalley Coulomb interactions (which are $\lesssim 1$ meV) such that the system only preserves a global spin SU(2) symmetry²⁹. Electron-phonon couplings can further break the $U_v(1)$ symmetry, which was proposed in REF.⁴³ as a possible mechanism for the correlated insulator states at the charge-neutrality point.

Depending on the specific stacking configuration, different moiré graphene systems may have different crystalline symmetries. However, when the moiré lattice constant is much greater than the atomic lattice constant, the microscopic lattice symmetries are not important and there are emergent symmetries on the moiré length scale that are captured by the continuum Hamiltonian. For example, for TBG, depending on the choice of the rotation centre, the symmetry group for the microscopic lattice can be D_6 (if the rotation centre is at the hexagon centre) or D_3 (if the rotation centre is at the carbon atom), but the low-energy continuum Hamiltonian describing the physics at the moiré length scale has the full D_6 symmetry regardless of the choice of the rotation centre¹⁰. Such emergent D_6 symmetry for the low-energy states of TBG has been numerically verified based on atomistic tight-binding calculations that include effects of structural relaxations⁶⁸. An important symmetry for TBG is the C_{2z} symmetry. Because both C_{2z} and time-reversal (T) would interchange the two valleys, the combined symmetry $C_{2z}T$ is a symmetry for each valley. If the graphene is aligned with an hBN substrate, both C_{2z} and $C_{2z}T$ symmetries would be broken by the substrate. In other moiré graphene systems such as twisted multilayer graphene and hBN-graphene systems, C_{2z} symmetry is typically broken in the intrinsic structure, allowing for valley-contrasting Berry curvatures and Chern numbers as discussed in detail in the section on topological properties of moiré graphene systems.

Experimental observations

Correlated insulators. Moiré and twisted graphene systems have attracted attention since 2018, thanks to the discoveries of the correlated insulating states and superconductivity in magic-angle TBG^{16,17}. As discussed above, for each valley of TBG there are two flat bands around the magic angle. Including the spin degeneracy, there are in total eight valley-spin-degenerate flat bands. When these flat bands are $\pm 1/2$ filled (that is, a filling of two electrons and/or holes with respect to the charge-neutrality

point (CNP)), the system is insulating with a thermal excitation gap of about 0.3 meV as indicated by the measured conductance (FIG. 2a)¹⁷. Superconducting domes emerge upon further doping the correlated insulating states around $\pm 1/2$ filling (FIG. 2b)¹⁶. Measurements of these phenomena have been reproduced⁴⁷. The measured longitudinal resistivity R_{xx} reported in REF.⁴⁷ exhibits sharp peaks at some integer filling factors $-1/2, 0, 1/2$ and $3/4$ ($\nu = -2, 0, 2$ and 3 in FIG. 2c). The magnitudes of these peaks decrease exponentially with respect to temperature, indicating that the system becomes insulating at these integer fillings. More interestingly, at $-1/2$ filling, the correlated insulating state exhibits the QAH effect with Chern number 2 in the presence of a weak vertical magnetic field of about 0.5 T (REF.⁴⁷). One possible explanation for such a striking phenomenon is some kind of flavour-polarized orbital ferromagnetic state with Chern number 2, which is stabilized by the external magnetic field^{69–71}. The correlated insulating phenomena in magic-angle TBG have been further verified by STM measurements, in which splittings of van Hove singularities at the CNP and other integer fillings have been observed^{49–52}. The splittings are indicated by dips of the differential conductance (dI/dV) at integer fillings (FIG. 2d), suggesting that the insulating behaviour is in fact driven by Coulomb interactions. More recently, a cascade of phase transitions have been observed at all integer fillings of TBG around the magic angle^{39,40}. STM and compressibility measurements also suggest that at integer fillings, the electrons tend to fully occupy an integer number of the fourfold degenerate flat bands, possibly lifting the flavour (valley and spin) degeneracy.

Correlated insulators have been observed in TDBG as well^{72–74}. Similar to TBG, TDBG also exhibits two flat bands for each valley and spin at small twist angles. These flat bands are topologically distinct for AB-AB and AB-BA stacking configurations^{28,32}. For AB-AB stacked TDBG, both the valley Chern numbers of the flat bands and their bandwidths can be tuned by vertical displacement fields^{28,29,32}. For example, with a perpendicular displacement field, the conduction flat band with reduced bandwidth would be energetically separated from the valence band, and correlated states may emerge when these isolated conduction flat bands are partially filled. In TDBG with twist angle 1.09° , resistivity peaks appear at the CNP and $1/2$ filling when the displacement field $|D|/\epsilon_0 \geq 0.18$ V nm⁻¹ (REF.⁷³)

(FIG. 2e) (ϵ_0 is the vacuum permittivity), which indicate the onset of the correlated insulator states. Similarly, when the twist

angle is 1.23° , correlated insulators emerge at the CNP, $1/4$ and $1/2$ fillings in the presence of finite displacement fields (FIG. 2f).

The gaps of the correlated insulating states increase in response to external magnetic field with a g factor $g \approx 1.5$, which implies

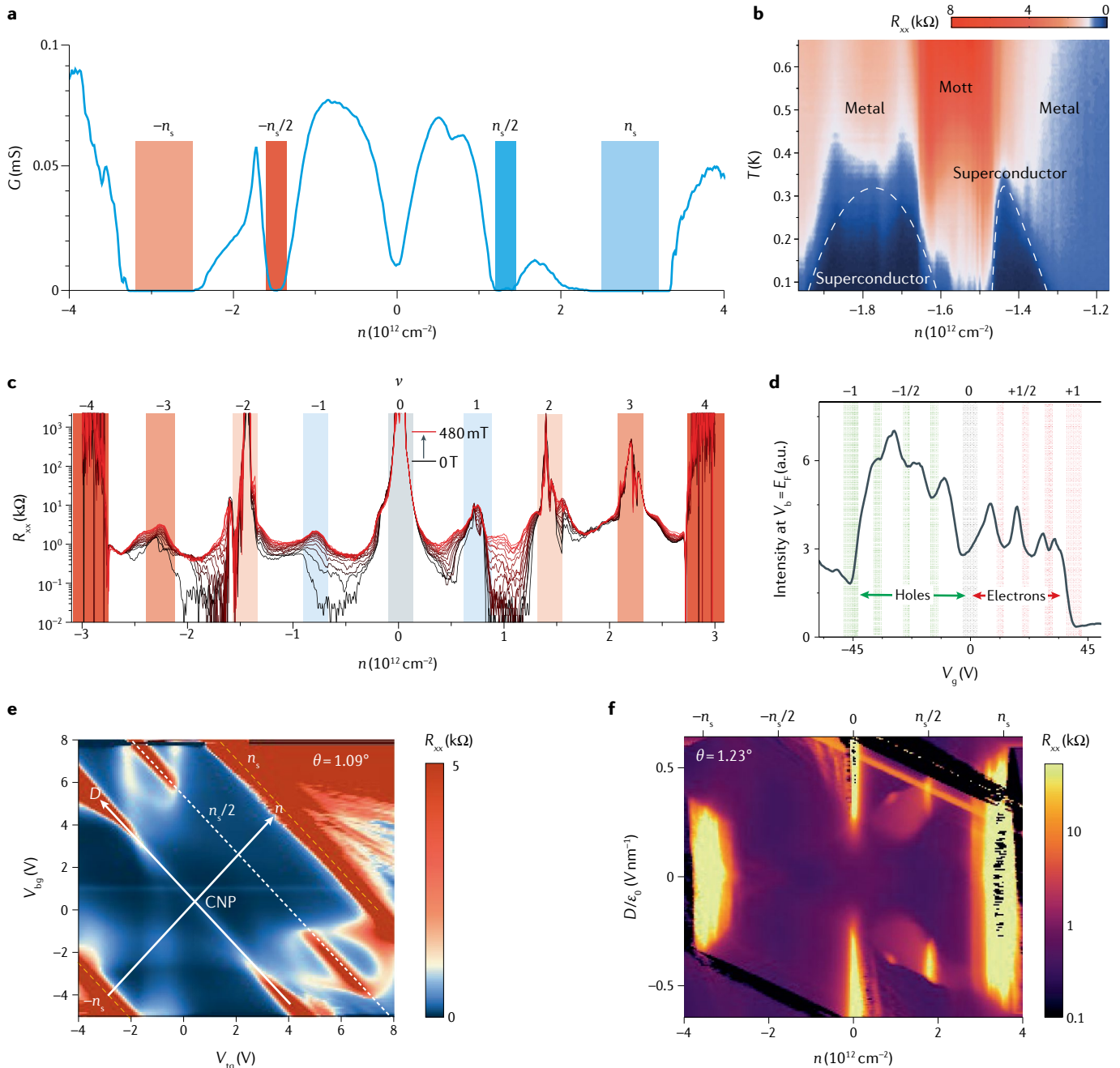


Fig. 2 | Correlated insulators in twisted graphene systems. **a** | Measured conductance (G) versus carrier density (n) in twisted bilayer graphene (TBG) at a twist angle of 1.08° . There are correlation-induced gaps at $\pm 1/2$ filling (indicated by darker shading). The lighter shaded gaps are the single-particle gaps between the flat bands and the remote bands. **b** | Measured longitudinal resistance (R_{xx}) near $-1/2$ filling in TBG at 1.16° as a function of filling and temperature (T). The correlated insulator at $-1/2$ filling is surrounded by superconducting domes. **c** | Measured longitudinal resistance versus carrier density in TBG at different perpendicular magnetic fields from 0 T (black line) to 480 mT (red line). Correlation-driven resistance peaks emerge at $-1/2$, 0, $1/2$, $3/4$ fillings as marked by the shaded regions ($\nu = -2, 0, 2, 3$ refers to number of charge carriers in each moiré primitive cell, where positive and negative ν stand for electron and hole carriers respectively). **d** | Measured differential conductance (dI/dV) intensity versus gate

voltage (V_g) (which is proportional to filling ν) at the chemical potential, in which dips of dI/dV appear at all integer partial fillings, that is, at 0, $\pm 1/4$, $\pm 3/4$, $\pm 1/2$. **e** | Measured R_{xx} of twisted double bilayer graphene (TDBG) at 1.09° versus top gate voltage (V_{tg}) and bottom gate voltage (V_{bg}). The carrier density and displacement field (D) are related to V_{tg} and V_{bg} by a linear transformation. Correlated insulator states are observed at 0 and $1/2$ fillings in finite displacement fields, $\pm n_s$, superlattice carrier density of four electrons/holes per moiré primitive cell; CNP, charge-neutrality point. **f** | Measured R_{xx} versus n and displacement field for TDBG at 1.23° . Correlated insulator states appear at 0, $1/4$ and $1/2$ fillings with finite displacement fields. ϵ_0 , vacuum permittivity. Part **a** adapted from REF.¹⁷ with permission. Part **b** adapted from REF.¹⁶ with permission. Part **c** adapted from REF.⁴⁷ with permission. Part **d** adapted from REF.⁵⁰ with permission. Parts **e**, **f** adapted from REF.⁷² with permission.

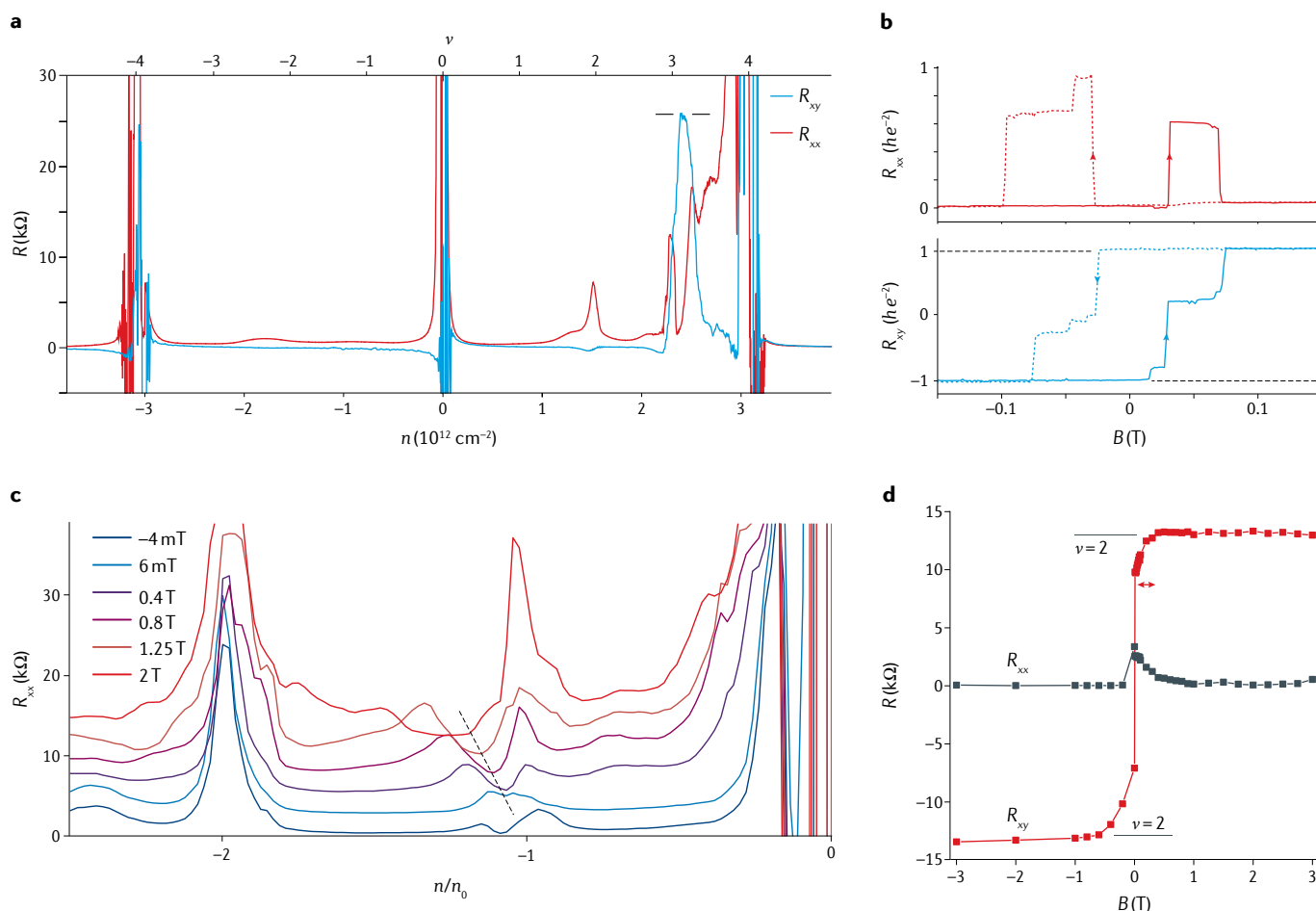


Fig. 3 | Quantum anomalous Hall effects in moiré graphene systems.

a | Longitudinal resistance (R_{xx}) and Hall resistance (R_{xy}) as a function of carrier density (n) in hBN-aligned (hBN, hexagonal boron nitride) twisted bilayer graphene (TBG) around a twist angle of 1.1° . R_{xy} reaches h/e^2 and R_{xx} approaches zero near $3/4$ filling, indicating a quantum anomalous Hall (QAH) insulating state. **b** | Hysteresis of R_{xx} and R_{xy} measured at $3/4$ filling as a function of magnetic field (B) for hBN-aligned TBG. **c** | Longitudinal

resistance of hBN-aligned trilayer graphene versus n , with displacement field $D/\epsilon_0 = -0.5 \text{ V nm}^{-1}$ and with different vertical magnetic fields. ϵ_0 , vacuum permittivity. **d** | Quantized Hall conductance with Chern number 2 is observed at $-1/4$ filling for $B \gtrsim 0.4 \text{ T}$. $\nu = n/n_0$, where n refers to the actual carrier density in the system and n_0 is the unit carrier density with one electron per moiré primitive cell. Parts **a,b** adapted from REF.²⁵ with permission. Parts **c,d** adapted from REF.¹⁰⁸ with permission.

that these correlated insulators may be spin polarized^{72–74}.

Orbital ferromagnetic states. The transport phenomena change strikingly when the TBG system is aligned with an hBN substrate. The longitudinal (R_{xx}) and transverse (R_{xy}) resistances for hBN-aligned TBG around the magic angle are reported in REF.²⁵. The longitudinal resistance reaches zero at $3/4$ filling (FIG. 3a), and the anomalous Hall resistance R_{xy} is quantized as h/e^2 with clear hysteretic behaviour (FIG. 3b), indicating the system is in a QAH insulating state with Chern number ± 1 at $3/4$ filling. Such a state is believed to be an orbital and spin ferromagnetic state with the unoccupied topological flat band split from the occupied ones^{41,45,46,75–77}. As discussed in detail in the next section, the QAH effect is crucially dependent on the C_{2z} -breaking induced by

the aligned hBN substrate. QAH effects with Chern number 2 has also been observed in hBN-aligned trilayer graphene system. The low-energy bands of ABC-stacked trilayer graphene have k^3 band touchings at the Dirac points K and K'. The moiré potential induced by the lattice mismatch between graphene and hBN would generate topological flat bands, where the valence flat bands exhibit valley Chern numbers ± 3 ^{27,36} (as discussed below). With a vertical displacement field of $D/\epsilon_0 = -0.5 \text{ V nm}^{-1}$, the topologically non-trivial valence flat band is pushed up in energy, which is separated from other bands by a substantial energy gap³⁶. At $-1/4$ filling and in the presence of a weak vertical magnetic field $|B| \gtrsim 0.4 \text{ T}$, the system becomes insulating as indicated by resistivity minima (FIG. 3c), with the anomalous Hall resistance R_{xx} quantized as $h/2e^2$ for $|B| \gtrsim 0.4 \text{ T}$ (FIG. 3d).

Correlated insulating states^{38,78,79} and QAH phenomena³⁸ have also been observed in twisted bilayer+monolayer graphene systems. For example, QAH states with Chern number 2 have been observed in a 1.25° twisted bilayer–monolayer system at $1/4$ and $3/4$ fillings in finite displacement fields³⁸. These QAH phenomena indicate that topologically non-trivial flat bands seem to be ubiquitous in moiré graphene systems. In the following section we discuss in detail the topological properties of these moiré graphene systems.

Topology in moiré sub-bands

The continuum model. To understand the intriguing phenomena observed in the various moiré graphene systems, one should first understand the non-interacting electronic structures and the corresponding topological properties. The low-energy band

structure of TBG is well described by the continuum Hamiltonian¹⁰

$$H_{\mu}^0 = \begin{pmatrix} -\hbar v_F(\mathbf{k} - \mathbf{K}_{\mu}^{\dagger}) \cdot \boldsymbol{\sigma}^{\mu} & U_{\mu}^{\dagger} \\ U_{\mu} & -\hbar v_F(\mathbf{k} - \mathbf{K}_{\mu}^{\mu}) \cdot \boldsymbol{\sigma}^{\mu} \end{pmatrix} \quad (1)$$

where $\boldsymbol{\sigma}^{\mu} = [\mu\sigma_x, \sigma_y]$, $\mu = \pm$ is the valley index, with $\mathbf{K}^- = \mathbf{K}$ and $\mathbf{K}^+ = \mathbf{K}'$. $U_{\mu}(\mathbf{r})$ denotes the moiré potential for the μ valley:

$$U_{\mu}(\mathbf{r}) = \begin{pmatrix} u_0 g_{\mu}(\mathbf{r}) & u' g_{\mu}(\mathbf{r} + \mathbf{r}_{AB}) \\ u' g_{\mu}(\mathbf{r} - \mathbf{r}_{AB}) & u_0 g_{\mu}(\mathbf{r}) \end{pmatrix} e^{-i\mu\Delta\mathbf{K} \cdot \mathbf{r}}, \quad (2)$$

where $\mathbf{r}_{AB} = (\sqrt{3}L_s/3, 0)$, and $\Delta\mathbf{K} = \mathbf{K}_2 - \mathbf{K}_1 = [0, 4\pi/(3L_s)]$. The inter-sublattice and intra-sublattice interlayer coupling parameters u_0 and u' can be derived from the graphene Slater–Koster tight-binding model⁶³, with $u_0 \approx 0.08$ eV and $u' \approx 0.098$ eV (REFS^{63,80}). The inter-sublattice coupling is stronger than the intra-sublattice coupling because of the effects of atomic corrugations⁸⁰. The phase factor $g(\mathbf{r})$ is defined as $g_{\mu}(\mathbf{r}) = \sum_{j=1}^3 e^{-i\mu\mathbf{q}_j \cdot \mathbf{r}}$, where $\mathbf{q}_1 = (0, 4\pi/3L_s)$, $\mathbf{q}_2 = (2\pi/\sqrt{3}L_s, 2\pi/3L_s)$ and

$\mathbf{q}_3 = (-2\pi/\sqrt{3}L_s, 2\pi/3L_s)$ are the three leading-order moiré wavevectors with dominant Fourier components of the moiré potential. In twisted multilayer graphene systems, the continuum Hamiltonians can be generalized based on Eq. (1) by replacing the diagonal blocks of Dirac fermions by multilayer graphene continuum Hamiltonians. In hBN-aligned graphene systems, the moiré potential comes from the hBN substrate and is exerted only on the bottom graphene layer. We refer the readers to REFS^{61,62} for more details.

Topological flat bands in TBG. The band structure of TBG at the first magic angle $\theta = 1.05^\circ$ can be obtained by diagonalizing the continuum Hamiltonian Eq. (1) in the plane-wave basis (FIG. 4a). The band structure can be calculated for both free-standing TBG, neglecting effects from the substrate, and TBG with a staggered sublattice potential $\Delta_M \sigma_z$ exerted on the bottom graphene layer, where σ_z is the third Pauli matrix in the sublattice space, and

$\Delta_M \approx 15$ meV models the effects from the alignment of hBN substrate^{45,46,81,82}. Without the sublattice potential ($\Delta_M = 0$), the Fermi velocities at \mathbf{K}_s and \mathbf{K}' vanish at the magic angle, and the overall bandwidth is less than 10 meV. The two flat bands for each valley are exactly degenerate at the \mathbf{K}_s and \mathbf{K}' points. The band degeneracy at an arbitrary point in the moiré BZ is topologically protected by $C_{2z}T$ symmetry of each valley, and is further pinned to the \mathbf{K}_s and \mathbf{K}' points owing to C_{3z} symmetry⁴². Note that the band structure of TBG from the continuum model exhibits a (approximate) particle–hole symmetry^{19,22,83}. Such an artificial particle–hole symmetry is absent in a more realistic atomic tight-binding model for TBG⁶³. If the effects of atomic corrugations (that is, a slow variation of the interlayer distance in the moiré pattern)⁵³ and other structural relaxations^{68,84} are included, the flat bands around the magic angle actually strongly break particle–hole symmetry^{68,84–86}.

More interestingly, the two flat bands for each valley are also topologically

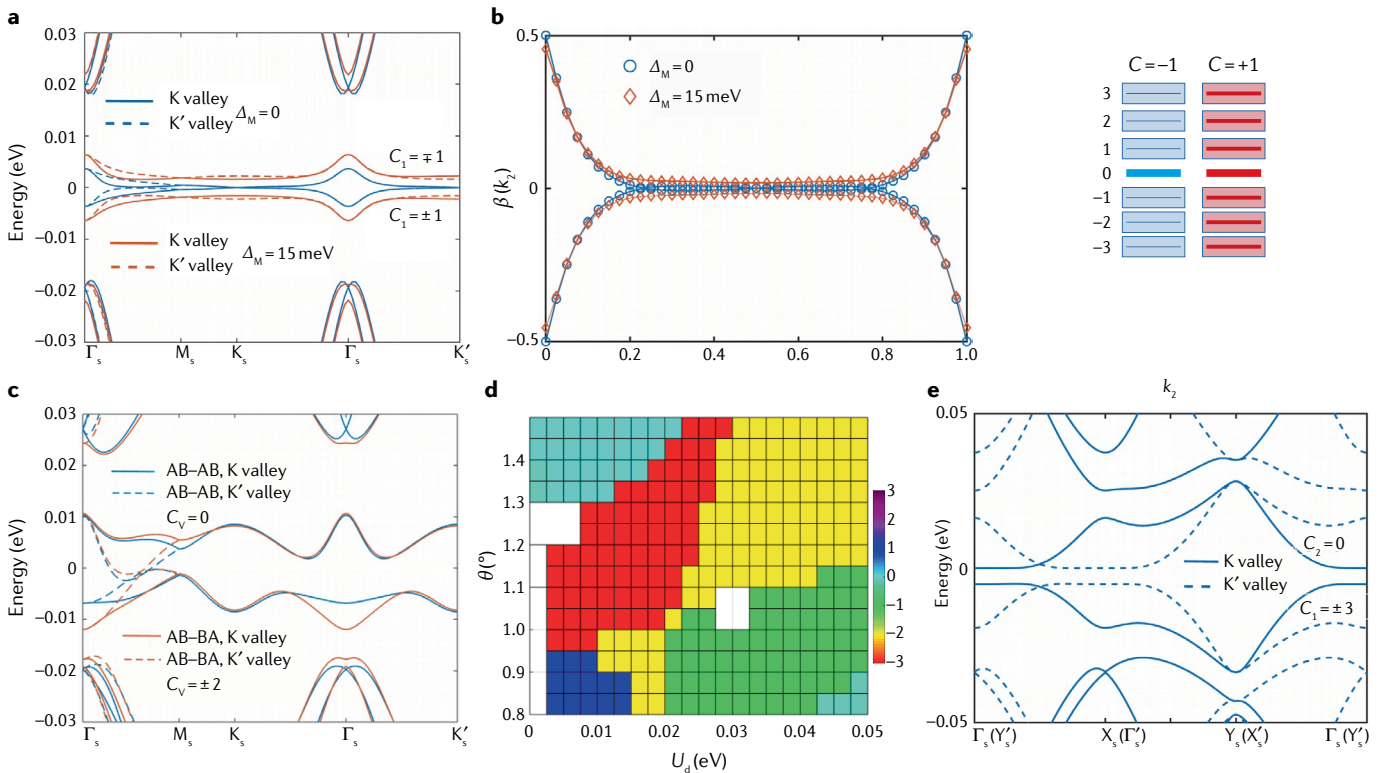


Fig. 4 | Band structures and topological properties of moiré graphene systems. **a** | Band structures for 1.05° twisted bilayer graphene (TBG) with (red lines) and without (blue lines) the staggered sublattice potential (Δ_M) induced by aligned hexagonal boron nitride (hBN) substrate. **b** | Wilson loops for the flat bands in magic-angle TBG with (red diamonds) and without (blue circles) the staggered sublattice potential. The inset illustrates the pseudo-Landau-level picture for TBG. k_z , momentum; $\beta(k_z)$, eigenvalue of the non-Abelian Berry phases at k_z ; C , Chern number. **c** | Band structures for twisted double bilayer graphene with AB–AB (blue) and AB–BA (red)

stackings at a twist angle of 1.24°. C_v , total valley Chern number of the two flat bands. **d** | Chern number of the conduction flat band of the K valley for twisted double bilayer graphene with AB–AB stacking, in the parameter space of twist angle θ and vertical electrostatic potential drop U_d . White regions are those in which the conduction flat band is degenerate with the valence flat band somewhere in the Brillouin zone, such that the Chern number for the conduction flat band is ill-defined. **e** | The band structures for hBN–trilayer graphene. Data replotted from REF.²⁷. In parts **a**, **c** and **e**, the solid and dashed lines represent the bands of K and K' valleys, respectively.

non-trivial in the sense that they exhibit similar topological character to that of a 2D \mathbb{Z}_2 topological insulator^{19–22}. In topological band theory, nearly all the topological properties of energy bands can be characterized by the Wilson loops, or the evolution of hybrid Wannier charge centres of the Bloch functions^{87–89}. The Wilson loops illustrate the non-Abelian Berry phases of the targeted group of Bloch functions integrated along one reciprocal vector direction (say, the k_1 direction), and one can extract the topological information of the Bloch functions by observing how the eigenvalues of the non-Abelian Berry phases evolve as k_2 increases from 0 to 1, where k_2 is the wavevector along the other reciprocal vector direction. This non-Abelian Berry phase can be denoted by $\beta(k_2)$. For a QAH insulator⁹⁰ with Chern number C , the sum of all the $\beta(k_2)$ would be changed by $2\pi C$ as k_2 increases from 0 to 1. Two-dimensional \mathbb{Z}_2 topological insulators or quantum spin Hall insulators^{91–94} can be intuitively interpreted as two copies of Chern insulators with two (pseudo) spin species exhibiting opposite Chern numbers ± 1 , which are connected to each other by a spinful time-reversal operation. Thus the Wilson-loop eigenvalues for the quantum spin Hall insulators consist of two copies with opposite Chern numbers ± 1 , which cross each other at the time-reversal invariant point $k_2 = 0$ or 0.5 . Interestingly, eigenvalues of the Wilson-loop matrix for the two flat bands of TBG for each spin each valley look exactly like those of a 2D quantum spin Hall insulator with odd winding pattern, with the degenerate points being protected by $C_{2z}\mathcal{T}$ symmetry^{19,20,22} (FIG. 4b). Moreover, such a non-trivial topological character can be trivialized by entangling remote bands with the flat bands and is thus dubbed ‘fragile topology’^{19–21,95,96}. Such fragile topology imposes obstructions in constructing symmetry-preserving and exponentially localized Wannier functions for the two flat bands^{42,95}. The topology in the band structure of TBG is surprising and puzzling, because it is well known that the non-trivial band topology in most existing topological materials results from SOC, but the atomic SOC for carbon is completely negligible.

The topological flat bands introduced above can also be understood from a different perspective, namely the pseudo-LLs caused by the artificial gauge field generated by the slowly varying moiré potential in the TBG system. The first gauge-field description for electronic states in TBG was proposed in REF.¹⁵, in which

the authors pointed out that such a gauge field is in general non-Abelian. Reference²² reports that in the AA stacking region of the moiré supercell, the above $SU(2)$ gauge field can be approximately reduced to two opposite $U(1)$ gauge fields in different subspaces, leading to pseudo-LLs around the centre of the AA region. After some appropriate unitary transformations, the continuum Hamiltonian for each valley can be expressed as

$$H^\mu(\mathbf{k}) = \begin{pmatrix} -\hbar v_F \left(\hat{\mathbf{k}} - \frac{e}{\hbar} \mathbf{A}^\mu \right) \cdot \boldsymbol{\sigma}^\mu & -3iu_0 \\ 3iu_0 & -\hbar v_F \left(\hat{\mathbf{k}} + \frac{e}{\hbar} \mathbf{A}^\mu \right) \cdot \boldsymbol{\sigma}^\mu \end{pmatrix} \quad (3)$$

where $\mathbf{A}^\mu = -\mu(2\pi u')/(L_s e v_F) [y, -x]$, with $\mu = \pm 1$ being the valley index. Without the off-diagonal $\pm 3iu_0$ term, the eigenenergies of Eq. (3) are simply the LLs of Dirac fermions, that is, $E_{N\pm k} = \pm \hbar \omega_c \sqrt{N}$ with $N \geq 0$ an integer and ω_c the cyclotron frequency. The two sets of pseudo-LLs in the Landau gauge for the upper (ϕ^u) and lower (ϕ^l) diagonal blocks of Eq. (3) are expressed as:

$$\begin{aligned} \phi_{N\pm k}^u(x, y) &= \frac{1}{\sqrt{2L_x l_B}} e^{ikx} \begin{pmatrix} \mp \Psi_N(\xi) \\ \Psi_{N-1}(\xi) \end{pmatrix} \\ \phi_{N\pm k}^l(x, y) &= \frac{1}{\sqrt{2L_x l_B}} e^{-ikx} \begin{pmatrix} \Psi_{N-1}(\xi) \\ \pm \Psi_N(\xi) \end{pmatrix}, \end{aligned} \quad (4)$$

where $\xi = y/l_B - l_B k$, and the corresponding cyclotron frequency and the magnetic length l_B are given by

$$\begin{aligned} \hbar \omega_c &= \sqrt{8\pi \hbar v_F u' / L_s}, \\ l_B &= \sqrt{(L_s \hbar v_F) / (4\pi u')}. \end{aligned} \quad (5)$$

The LLs for Dirac fermions in graphene possess an interesting property: the zeroth LL is 100% sublattice polarized, and for opposite magnetic fields the zeroth LL exhibits exactly opposite sublattice polarizations⁹⁷. Because the upper and lower diagonal blocks of Eq. (3) are Dirac fermions coupled to opposite pseudo-magnetic fields, the two zeroth pseudo-LLs with opposite chiralities and opposite sublattice polarizations eventually evolve to two flat bands with opposite Chern numbers ± 1 when the full periodic moiré potential is taken into account. Including the off-diagonal terms $\pm 3iu_0$ would allow the two sets of pseudo-LLs to be coupled together, but it should be noted that the $\pm 3iu_0$ coupling term is intra-sublattice, and would be vanishing in the subspace of the two

zeroth pseudo-LLs with exactly opposite sublattice polarizations. It follows that the higher pseudo-LLs can be coupled together, forming some entangled bands, and would lose their topological character, but the two zeroth pseudo-LLs would remain flat and retain their non-trivial topology. This is the origin of the non-trivial band topology for the flat bands in TBG.

It is interesting to note that the pseudo-magnetic fields are generated by the intersublattice moiré potential u' ; thus, increasing u' would enhance the pseudo-LL spacing ($\hbar \omega_c$ in Eq. (5)); the intra-sublattice moiré potential u_0 tends to couple the two sets of pseudo-LLs, reducing the gap between the zeroth and higher pseudo-LLs. Therefore, when atomic corrugations are taken into account⁹⁸, u' becomes larger than u_0 (REF.⁸⁰), which opens up a gap between the flat bands and high-energy bands. When the intra-sublattice coupling u_0 vanishes, the system has a chiral symmetry. In such a chiral approximation, at the magic angle the flat bands become exactly flat at zero energy²³, protected by the chiral symmetry.

Moreover, it follows from Eq. (4) that in the subspace of the zeroth pseudo-LLs (for each valley) the $C_{2z}\mathcal{T}$ operator is represented by $i\sigma_y \mathcal{K}$, where σ_y is the Pauli matrix in the sublattice space and \mathcal{K} is complex conjugation. Therefore, for the two zeroth pseudo-LLs of each valley, $C_{2z}\mathcal{T}$ operation behaves exactly as a spinor time-reversal operation with $(C_{2z}\mathcal{T})^2 = -1$, which protects the Kramers-like degeneracy of the zeroth pseudo-LLs for each valley. Once the $C_{2z}\mathcal{T}$ symmetry for each valley is broken, the two flat bands around K_s and K' are no longer degenerate. This can be seen in the splitting of the degeneracy points at K_s and K' points when a staggered sublattice potential $\Delta_M = 15$ meV is applied to the bottom layer (FIG. 1a). Similarly, the $C_{2z}\mathcal{T}$ -breaking staggered sublattice potential from the hBN substrate opens gaps in the Wilson-loop eigenvalues at $k_2 = 0$ and $k_2 = 0.5$ (FIG. 4b).

It is worth noting that Eq. (3) results from a linear expansion of r/L_s centred at the AA region. Therefore, the pseudo-LL picture applies only to the states in the AA region, which are those around the K_s and K' points in the moiré BZ⁹⁹. Accordingly, the doubly degenerate states around the K_s and K' points for each valley can be represented by the zeroth pseudo-LLs, which have vanishing Fermi velocities at the magic angle. However, Eq. (3) involves (pseudo-) vector potentials that are linear in \mathbf{r} , and thus fails to describe the states in the AB/BA

regions of the moiré pattern and does not preserve the moiré translational symmetry. It is natural to ask whether the pseudo-LL states discussed above are still robust if one keeps all orders of the moiré potential. Such a problem has been resolved in REF.²³, which reports analytic solutions for the eigenstates of the continuum model in the ‘chiral limit’ with the intra-sublattice moiré potential $u_0 = 0$. At the first magic angle, the two low-energy bands for each valley are exactly flat in the entire moiré BZ²³, and the eigenstates are highly reminiscent of the lowest LL wavefunctions on a torus¹⁰⁰. Actually, the eigenstates for the exactly flat bands in the chiral limit can be considered as a type of generalized lowest LL states, generated by Dirac fermions coupled to inhomogeneous pseudo-magnetic fields that have moiré translational symmetry¹⁰¹. The exact expression for the inhomogeneous pseudo-magnetic field $B(\mathbf{r})$ (in the chiral limit) is given in REF.¹⁰¹; $B(\mathbf{r})$ is approximately homogeneous in the AA region, drops rapidly as \mathbf{r} approaches the AB/BA region and eventually flips sign near the AB/BA points. These discussions imply that the non-trivial topological character stemming from the pseudo-magnetic fields are retained even if the higher-order intra-sublattice moiré potential terms are included.

The non-trivial topological character of the flat bands in TBG is important in determining how the eigenenergies of the system evolve in response to external magnetic fields, in other words, the ‘Hofstadter butterfly’¹⁰². Because the moiré potential generates opposite pseudo-magnetic fields in the moiré pattern, an external magnetic field would enhance the pseudo-magnetic field in one direction and diminish it in the opposite direction. Therefore, the pseudo-LL spacing for the Dirac fermions would increase for the pseudo-magnetic field aligned with the external magnetic field and decrease for the pseudo-magnetic field opposite to the external field. As a result, the LLs from the flat bands and from the high-energy bands would tend to be connected to each other if the external magnetic field is large enough. Such a picture has been independently proposed from the perspective of fragile topology of the TBG flat bands and has been verified by directly calculating the Hofstadter energy spectra¹⁰³. Moreover, it has been shown that for a superconductor with topologically non-trivial flat bands characterized by the non-zero spin Chern numbers, its superfluid weight can be expressed as

the BZ integral of the ‘quantum distance’ of the Bloch states, which is bounded by the spin Chern number¹⁰⁴. Because the two flat bands in magic-angle TBG can be viewed as the two zeroth pseudo-LLs with opposite chiralities, the superfluid weight for the flat bands in magic-angle TBG also has substantial contributions from the quantum geometry of the flat-band Bloch functions^{105–107}, which have a lower bound given by the winding number of the Wilson loops protected by $C_{2z}\mathcal{T}$ symmetry¹⁰⁷. If an hBN substrate is aligned with TBG such that the C_{2z} symmetry (sublattice symmetry) is broken by the substrate, $C_{2z}\mathcal{T}$ symmetry is no longer preserved for each valley. As a result, a valley-polarized ground state may have non-zero Chern number and exhibit the (quantum) AHE as already observed at 3/4 filling^{24,25}.

Flat bands in other moiré graphene systems.

Flat bands with non-trivial band topology are not unique to TBG. Flat bands with non-zero valley Chern numbers generically exist in twisted multilayer graphene systems and in other moiré graphene systems. For example, in TDBG there are relatively flat bands for a wide range of twist angles θ . AB/BA-stacked bilayer graphene has two kinds of stacking chiralities, the AB and BA stackings. If the twisted double bilayers are AB–AB stacked, then the total valley Chern number of the two flat bands is zero for most twist angles^{28,32}; if the two bilayers are AB–BA stacked, then the total valley Chern number of the two flat bands is ± 2 (REFS^{28,32}). The valley Chern numbers of these flat bands can also be tuned by vertical displacement fields^{27–29,32}. The band structures of TDBG at $\theta = 1.24^\circ$ are similar for the two different stacking configurations (FIG. 4c), but the total valley Chern number of the two flat bands in AB–AB stacked TDBG is zero, whereas it is ± 2 for the AB–BA stacking.

Indeed, if one only considers nearest-neighbour interlayer hopping in the chiral graphene multilayers, there are always two flat bands with vanishing Fermi velocities at the magic angle $\theta = 1.05^\circ$ for generic twisted chiral multilayer graphene systems, in which N chiral graphene layers are placed on top of M chiral graphene layers and twisted with respect to each other by θ (REF.²⁸). The total valley Chern numbers of the two flat bands in such $(M+N)$ twisted graphene multilayers are generically non-zero, and can be succinctly described by the following equation in the chiral approximation (keeping only the nearest-neighbour interlayer coupling):

$$C_{\alpha,\alpha'}^{K\mu} = -\mu(\alpha(M-1) - \alpha'(N-1)),$$

where $C_{\alpha,\alpha'}^{K\mu}$ denotes the total Chern number of the two low-energy flat bands for the μ valley, and the subscripts $\alpha, \alpha' = \pm 1$ represent the stacking chiralities of the M layers and N layers, with $\alpha, \alpha' = +1$ for AB stacking and $\alpha, \alpha' = -1$ for BA stacking.

Equation (6) is no longer exact when further-neighbour interlayer coupling terms are included. However, the total of the valley Chern numbers of the two flat bands is a more robust quantity than that of each flat band. The former is unchanged as long as the two flat bands remain energetically separated from the remote high-energy bands. Moreover, the valley Chern numbers are highly tunable by vertical displacement fields. FIGURE 4d shows the Chern number of the conduction flat band for the K valley of AB–AB stacked TDBG in the parameter space of the twist angle θ and the vertical electrostatic potential energy drop across the four layers (U_d). At different θ and U_d , the Chern number of the conduction flat band of the K valley can be 0, ± 1 , -2 or -3 , which provides a rich platform to study the interplay between non-trivial topology and strong Coulomb correlations.

Topological flat bands with non-zero valley Chern numbers also exist in chiral graphene multilayers aligned with an hBN substrate^{27,35,36}. The moiré potential in hBN–graphene system is generated by the lattice mismatch between graphene and hBN layers. As a result, the moiré BZ is rotated by 90° compared with that of TBG, and the moiré BZs for the K and K' valleys are horizontally shifted by $4\pi/(3L_c)$ with respect to each other. In hBN-aligned ABC trilayer graphene, the valence flat band acquires a non-zero valley Chern number ± 3 due to the moiré potentials generated by the hBN substrate (FIG. 4e). If the valley symmetry or orbital time-reversal symmetry is spontaneously broken at some integer fillings of the flat bands, the hBN–trilayer system would stay in an orbital ferromagnetic state that exhibits a (quantum) AHE. Indeed, a quantized anomalous Hall conductivity with Chern number 2 has been observed at 1/4 filling of the valence band in hBN-aligned trilayer graphene¹⁰⁸. The system is believed to stay in a spin-valley-polarized insulating state at 1/4 filling, and the band structure for each valley each spin is strongly renormalized by Coulomb interactions such that the Chern number of the valence band is changed from 3 to 2 (REF.¹⁰⁸).

Moiré orbital magnetic states

The non-trivial topological properties of the moiré flat bands imply that moiré graphene systems are closely related to orbital magnetism. In TBG, it has been discussed above that the two flat bands with opposite Chern numbers (for each valley) are derived from the two zeroth pseudo-LLs: thus, the ground state of each valley is expected to exhibit a current pattern with opposite circulating current loops, owing to the cyclotron motions of Dirac fermions driven by the opposite pseudo-magnetic fields. The current density distribution should preserve the C_{2z} , C_{3z} and C_{2x} symmetries in the moiré supercell, giving rise to the three pairs of compensating current loops in each moiré supercell (FIG. 5a). Such compensating current loops give rise to a staggered orbital magnetizations on the moiré length scale⁴¹. If the TBG system is aligned with an hBN substrate, a staggered sublattice potential is imposed on the graphene in the AA regions, which opens up a gap at the Dirac points K_s and K' , giving rise to non-zero valley Chern numbers. In this case, each valley breaks C_{2z} symmetry, which allows for non-zero and valley-contrasting orbital magnetizations.

If \mathcal{T} symmetry is spontaneously broken at some partial fillings of the flat bands, the resulting valley-polarized state would be an orbital ferromagnetic state with a non-vanishing (even quantized) AHE. Such a scenario has been suggested by several theoretical groups as the mechanism that gives rise to the QAH effect at 3/4 fillings in hBN-aligned magic-angle TBG^{41,45,46,76}. Such moiré orbital ferromagnetic states are associated with chiral current loops circulating around the AA regions of the moiré pattern (FIG. 5b)⁴¹. The characteristic radius of the current loop is of the order of the moiré length scale L_s , which is associated with large orbital angular momentum $L_z = \mathbf{r} \times \mathbf{p}$, with $|\mathbf{p}| \sim \hbar k$ and $|\mathbf{r}| \sim L_s \gg a$. Therefore, the orbital magnetization generated by the current loops on the moiré scale is expected to be much greater than that on the microscopic lattice scale²⁸. As a result, an orbital ferromagnetic state in the moiré graphene system would exhibit a notable Zeeman effect contributed by the giant orbital magnetization^{28,41,45,46,109}. For example, the calculated orbital magnetization is approximately 2–10 μ_B (REFS^{41,45,46}) per moiré primitive cell in the QAH state at 3/4 filling in hBN-aligned TBG.

The orbital ferromagnetic state has been directly confirmed by spatially resolved magnetometry in hBN-aligned TBG at the magic angle at 3/4 filling; the measurements suggest that the orbital magnetization is of the order of several Bohr magnetons per unit carrier density¹¹⁰. An orbital ferromagnetic state is also observed by STM measurements in a non-magic TBG system at $\theta = 1.68^\circ$ with a multilayer graphene substrate, in which a linear-in-field valley splitting has been observed, implying an orbital moment as large as about 10 μ_B per moiré supercell¹¹¹.

The orbital magnetization contributed by the flat bands of the K valley¹⁰⁹ varies linearly with respect to the chemical potential in the bulk CNP gap (FIG. 5c). This linear dependence is caused by the ‘itinerant circulation’ from the gapless edge states^{112,113}.

Non-zero valley Chern numbers and the large valley-contrasting orbital magnetizations also exist in twisted multilayer graphene and hBN-aligned multilayer graphene systems. In TDBG with AB–AB stacking, the system breaks C_{2z} symmetry intrinsically, but still preserves C_{2x} symmetry, which enforces the orbital magnetization of each valley to be vanishing. C_{2x} symmetry can be broken by a vertical displacement field, giving rise to non-zero valley Chern numbers and valley-contrasting orbital magnetization. However, in TDBG with AB–BA stacking the system has C_{2y} symmetry, which interchanges the two valleys. Although C_{2y} symmetry enforces the total orbital magnetization to be zero, it still allows for non-zero and opposite orbital magnetizations from the two valleys^{28,29,32} (FIG. 5d). In hBN-aligned chiral multilayer graphene systems, the moiré potential from the lattice mismatch between hBN and graphene is also expected to give rise to topological flat bands with non-zero valley Chern numbers^{27,36}, valley-contrasting orbital magnetizations and chiral current loops in real space.

The mechanisms of the (quantum) AHE in the orbital ferromagnetic states of moiré graphene systems are distinct from those in conventional spin magnetic systems or spin–orbit coupled magnetic systems. In spin–orbit coupled systems, the AHE results from the interplay between spin magnetism and SOC¹¹⁴; first, \mathcal{T} symmetry is broken in the spin sector, leading to spin magnetizations, then SOC transmits the \mathcal{T} symmetry breaking from the spin sector to the orbital sector. In orbital ferromagnetic systems, however, microscopic SOC is not necessary for the AHE if \mathcal{T} symmetry is directly broken in the orbital sector. Accordingly,

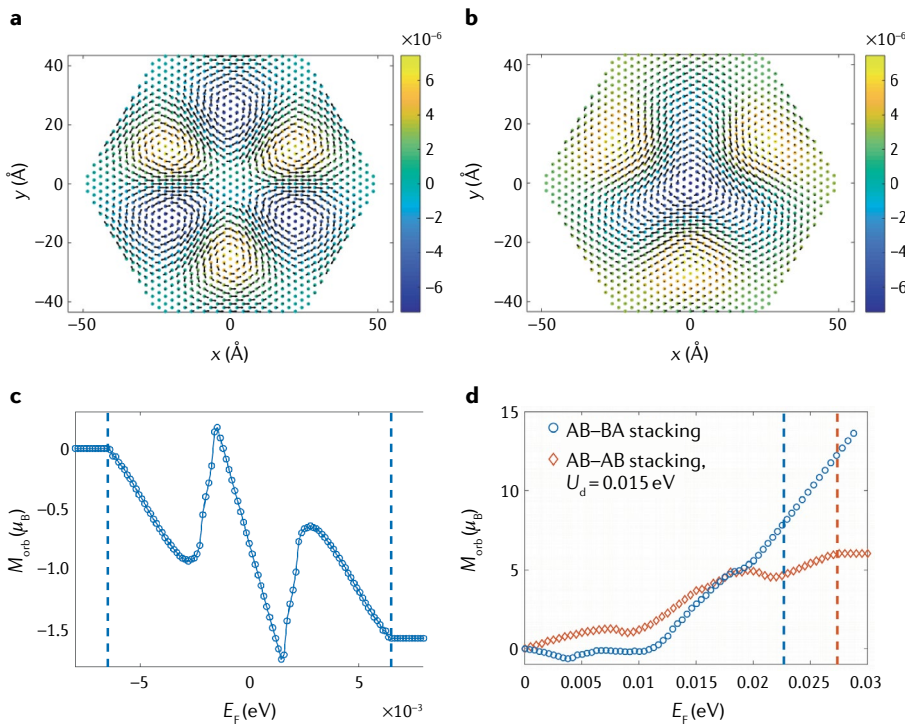


Fig. 5 | Moiré orbital ferromagnetism. **a, b** | Real-space current density distribution contributed by the K-valley flat bands of magic-angle twisted bilayer graphene (TBG) with staggered sublattice potential $\Delta_M = 0$ (part **a**) and $\Delta_M = 15$ meV (part **b**). **c** | Orbital magnetization (M_{orb}) contributed by the K-valley flat bands of magic-angle TBG with $\Delta_M = 15$ meV, plotted against the Fermi level (E_F). **d** | Orbital magnetizations for AB–AB stacked double bilayer graphene (TDBG) with vertical potential energy drop $U_d = 0.015$ eV (red diamonds) and for AB–BA stacked TDBG (blue circles). The vertical dashed lines in parts **c** and **d** mark the band edges of the flat bands.

the AHE in an orbital ferromagnetic system is expected to be far more conspicuous than in a spin ferromagnetic system. Conversely, in a spin magnetic system the SOC is typically much smaller than the bandwidth; thus, the anomalous Hall conductivity is much smaller than the diagonal conductivity¹¹⁴.

A similar argument also applies to magneto-optical effects. Because light couples directly to the orbital degrees of freedom of electrons, the magneto-optical effects in an orbital ferromagnet should be much more pronounced than those in a spin ferromagnet. Therefore, significant magneto-optical responses are also expected in the orbital ferromagnetic states of moiré graphene systems, especially in the terahertz frequency regime¹¹⁵. Moreover, because the magnetization in an orbital magnetic state is generated by the orbital motions (current loops) of electrons, which are directly coupled to external electric fields, the out-of-plane orbital magnetization can thus be controlled, even switched, using in-plane electric fields^{25,38,116–119}.

Inversion symmetry can be broken in some moiré graphene systems such as hBN-aligned TBG and TDBG, allowing for nonlinear optical effects such as shift current and second-harmonic generations^{120,121}. It is intriguing to ask whether the orbital magnetization and valley polarization in twisted graphene systems can be probed by nonlinear optical responses. By virtue of the flat bands and the small excitation gaps, hBN-aligned TBG and TDBG systems are expected to exhibit giant nonlinear optical responses in the terahertz and infrared frequency regime¹¹⁵. Some components of the nonlinear photoconductivity tensor are directly proportional to the orbital magnetization of the system, enabling the detection of orbital ferromagnetic states by nonlinear optics¹¹⁵. It is also interesting to note that it is theoretically proposed¹²² that circular polarized light can induce a static out-of-plane electric dipole moment through the nonlinear layer circular photogalvanic effect.

Correlated insulators in TBG

As discussed above, several theoretical groups have proposed that the QAH effects in moiré graphene systems with broken C_{2z} symmetry result from the interaction-driven spontaneous-symmetry-breaking phases, which split the otherwise degenerate flat bands and open gaps with non-zero Chern numbers^{22,35,41,45,46,75–77}. What remains mysterious is the seemingly ‘featureless’ correlated insulating states at $\pm 1/2$ fillings and at the CNP of the flat bands in TBG

at the magic angle. A TBG system that is not aligned with a hBN substrate has been reported¹⁷, and the system is considered to preserve C_{2z} symmetry on the moiré length scale. The correlated insulating states at $\pm 1/2$ fillings and the CNP exhibit vanishing anomalous Hall conductivity, indicating that the ground states preserve C_{2z} symmetry. Various theories have been proposed to explain the nature of the peculiar correlated insulating states^{42,44–46,75–77,80,99,123–140}. Most of these theories are based on moiré-scale real-space lattice tight-binding models^{42,80,99,123,126–130,138,139,141}, some others start from weak-coupling analysis based on ‘hot-spot’ models near the van Hove singularity¹⁴² around $\pm 1/2$ filling^{125,143}, and others are directly based on the continuum Hamiltonian expanded in the plane-wave basis with the Coulomb interactions treated by the Hartree–Fock approximation^{44,76,77,131,133,135} or other numerical approaches such as density matrix renormalization group^{140,144}. Despite extensive theoretical studies from various perspectives, the essence of these correlated insulating states is still under debate.

Several physicists in this field, including us, hold the perspective that the correlated insulating states observed in TBG, and some other moiré graphene systems with topologically non-trivial flat bands, are not Mott insulators. Instead they result from spontaneous symmetry breaking of flavour (valley and spin) and/or lattice symmetries^{22,37,41,44,45,69–71,76,77,131,140}, driven by the exchange part of the Coulomb interactions projected onto the Dirac fermions with valley, spin and sublattice degrees of freedom^{41,44,76,77,131}. The rationale for this perspective is that topologically non-trivial flat bands are ubiquitous in moiré graphene systems, and the non-trivial topology imposes strong obstructions to constructing exponentially localized and symmetry-preserving Wannier functions (only) for the flat bands, which impedes a real-space description of the flat bands based on well localized orbitals like the Hubbard model. Instead, the correlation problem in magic-angle TBG resembles that of quantum Hall ferromagnetism^{22,23,44,45}. Such degeneracy can be lifted at partial integer fillings by the exchange part of Coulomb interactions, giving rise to a correlated insulating state from spontaneous symmetry breaking.

Such ideas have been numerically explored by Hartree–Fock calculations based on the continuum model. In principle, one needs to consider the total Hamiltonian

$H = H_0 + H_C$, where H_0 is the non-interacting continuum Hamiltonian, and H_C is the Coulomb interaction, which can be expressed in momentum space as

$$H_C = \frac{1}{2N_s} \sum_{\alpha\alpha'} \sum_{\mathbf{k}\mathbf{k}'} \sum_{\mathbf{q}} V(\mathbf{q}) \hat{c}_{\mathbf{k}+\mathbf{q},\alpha\sigma}^\dagger \hat{c}_{\mathbf{k}-\mathbf{q},\alpha'\sigma'}^\dagger \hat{c}_{\mathbf{k}',\alpha'\sigma'} \hat{c}_{\mathbf{k},\alpha\sigma} \quad (6)$$

where \mathbf{k} is the wavevector of the Dirac fermion in the BZ of monolayer graphene, α is the combined layer and sublattice index, and σ is the spin index. $c_{\mathbf{k},\alpha\sigma}^\dagger$ and $c_{\mathbf{k},\alpha\sigma}$ represent the creation and annihilation operators of the Dirac fermions. N_s is the total number of moiré supercells in the entire system. $V(\mathbf{q})$ is the Fourier transform of the Coulomb interaction, which typically takes some empirical screened form. For example, in REFS⁴¹ and⁷⁷, $V(\mathbf{q})$ takes a Thomas–Fermi screening form $V(q) = e^2 / (4\pi\epsilon \sqrt{q^2 + \kappa^2})$ with two empirical parameters: a background dielectric constant ϵ and an inverse screening length κ . Hartree–Fock phase diagrams at different fillings of TBG in the parameter space of (κ, ϵ) have been constructed⁴¹. In some other works, $V(\mathbf{q})$ is taken to be in the single-gate^{76,133} or double-gate screened form⁴⁴. However, the different screening forms of Coulomb interactions $V(\mathbf{q})$ actually have the same asymptotic behaviour for small q and large q ; thus, it is expected that the qualitative features of the ground states of TBG should be independent of the specific choice of the screening form of the Coulomb interactions.

For hBN-aligned TBG, Hartree–Fock calculations from several theoretical groups^{41,45,46,76,77,140} indicate that the ground states at $\pm 3/4$ fillings are actually valley- and spin-polarized QAH states with Chern number ∓ 1 , a result which is consistent with transport measurements reported in REF.²⁵. The Hartree–Fock results are further substantiated by unbiased many-body numerical calculations using density matrix renormalization group¹⁴⁰ and exact diagonalizations^{136,145}, which confirm that a fully valley- and spin-polarized state with Chern number ± 1 is favoured at $3/4$ filling. Moreover, because the Chern numbers at hole and electron fillings are opposite for the same valley polarization, it has been theoretically proposed that the QAH states at electron and hole fillings of hBN-aligned TBG would exhibit hysteresis loops with opposite chiralities⁴¹.

QAH effects with different Chern numbers at various integer fillings have also been observed in TBG without an aligned hBN substrate, but rather in the presence

of (weak) vertical magnetic fields^{69–71,146,147}. These QAH states with different Chern numbers have been reported to be observed through direct transport measurements that show quantized Hall conductivities^{69,70,146,147}. In another approach, the Chern numbers of the QAH states are determined by the slope dn/dB (where n is charge density) through STM measurements⁷¹. In all these works, QAH states with Chern number ± 1 , ± 2 and ± 3 have been observed at $\pm 3/4$, $\pm 1/2$ and $\pm 1/4$ fillings with finite-onset magnetic fields $B \approx 0.3\text{--}7\text{ T}$.

Although there are different perspectives for the QAH phenomena discussed above^{148,149}, here we present a simple picture that can succinctly explain these phenomena through the analogy between the topological flat bands and the zeroth pseudo-LLs^{22,23,41,45,46,69,145}. Including the valley and spin degrees of freedom, there are in total eight flat bands at the first

magic angle. These flat bands are exactly dispersionless in the chiral limit at the magic angle²³. These eight topological flat bands derived from the zeroth pseudo-LLs exhibit opposite Chern numbers ± 1 , opposite spin indices and (approximately) opposite sublattice polarizations^{22,23,45} (FIG. 6). If the Coulomb interactions and the hBN substrate are both absent, all eight topological flat bands are degenerate (FIG. 6a). Aligning the TBG with an hBN substrate would impose a staggered sublattice potential, which opens a gap of about 4 meV between the flat bands with A and B sublattice polarizations; the gap can be significantly enhanced by Coulomb interactions. At $-3/4$ filling, only one of the four pseudo-LLs with the lower-energy sublattice polarization is occupied; at $+3/4$ filling, only one of the four pseudo-LLs with the higher-energy sublattice polarization is unoccupied. The exchange Coulomb interactions would

open a gap between the occupied and unoccupied topological flat bands with ± 1 Chern numbers, leading to a valley- and spin-polarized state with $C = \pm 1$ (FIG. 6b). When a weak magnetic field is present, the eightfold degenerate topological flat bands can be split by the orbital Zeeman effect, which splits the four flat bands with $C = +1$ from those with $C = -1$. The four degenerate $C = +1$ flat bands (for electron filling) are partially occupied, and exchange gaps are opened up at $3/4$, $1/2$ and $1/4$ integer fillings, leading to QAH states with Chern number 1, 2 and 3 (FIG. 6c–e)^{69–71}.

The above discussions indicate that the QAH insulator states observed in TBG, either aligned with hBN substrate²⁵ or coupled with external magnetic fields^{69–71,146,147}, arise from spontaneous breaking of valley and/or spin symmetries of the eight topological flat bands in the non-interacting continuum Hamiltonian. Although the detailed mechanisms may still require further study, it seems that the aligned hBN substrate and the external magnetic fields tend to drive the system into spontaneous-symmetry-breaking states, and the Chern numbers of the insulating states can be obtained simply by counting the contributions from the occupied Chern bands.

The correlated insulator states observed in TBG without hBN alignment are much more elusive. In a realistic situation, the bandwidth of the two low-energy bands per spin per valley is about 10 meV around the magic angle, which is comparable to the Coulomb repulsion energy on the moiré scale of about 25 meV (assuming a background dielectric constant of 4). Therefore, the kinetic energy and the details of the low-energy band structure, such as the Dirac points in the moiré BZ and the van Hove singularities, play crucial roles in determining the actual ground states at different fillings of TBG. These details are beyond the simplified pseudo-LL picture or the chiral limit with exactly flat bands. To understand the nature of the correlated insulator states observed in a realistic TBG device, one has to resort to numerical calculations. As a starting point, one would naturally make Hartree–Fock approximations to the Coulomb interactions.

Hartree–Fock calculations from different groups indicate that the nature of the ground states for magic-angle TBG are sensitive to the approximations used and specific treatments of Coulomb interactions. For example, REF.¹³¹ reports a study in which Coulomb interactions were projected onto

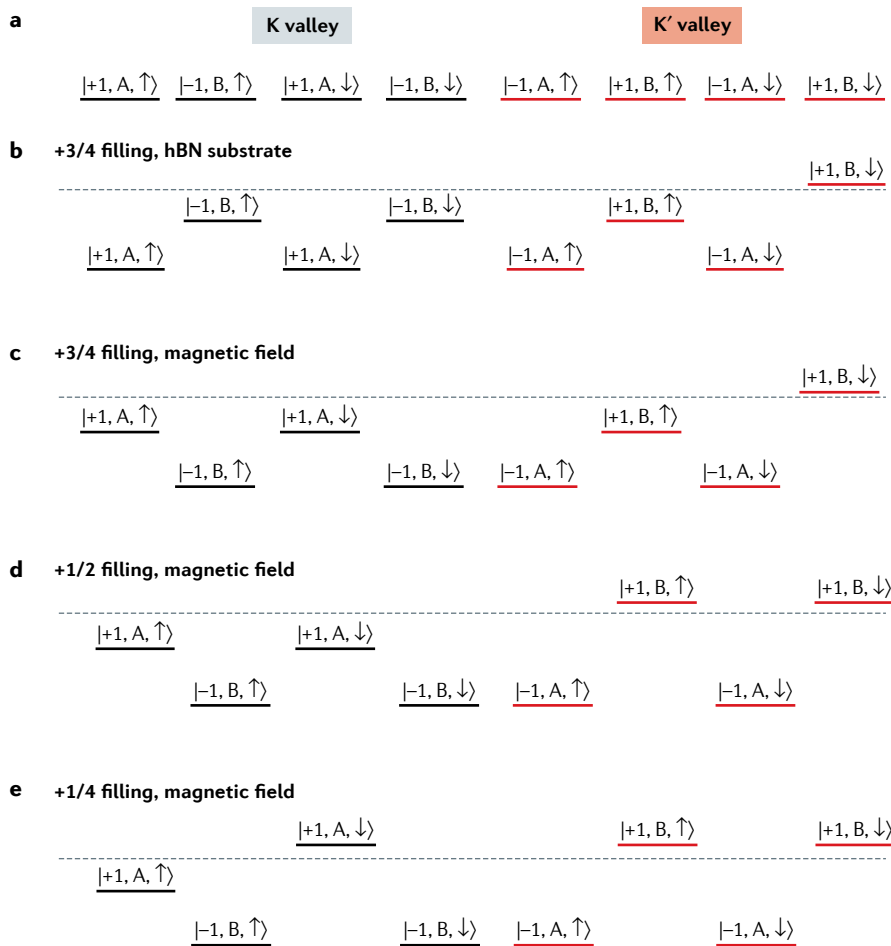


Fig. 6 | A pseudo-Landau-level picture for twisted bilayer graphene (TBG). **a** | The eight degenerate flat bands with opposite Chern numbers, spins and sublattice polarizations. **b** | Schematic of quantum anomalous Hall states with Chern number 1 at $3/4$ filling in hexagonal boron nitride (hBN)-aligned TBG. **c–e** | Schematic illustrations of quantum anomalous Hall states at $3/4$ filling (part **c**), $1/2$ filling (part **d**) and $1/4$ filling (part **e**) in the presence of magnetic fields. Figure adapted from REF.⁶⁹ with permission.

the flat bands and Hartree–Fock calculations were performed for the flat bands in the layer-sublattice space. This study led to the conclusion that the ground states at CNP are likely to be sublattice polarized states that break C_{2z} symmetry, and thus break $C_{2z}\mathcal{T}$ symmetry for each valley. If a flavour polarization is present, the state discussed in REF.¹³¹ could be a QAH insulator¹³¹.

In one of these papers, Hartree–Fock calculations have been reported⁴⁴ that include some of the remote bands, leading to the conclusion that the ground state at CNP is a Kramers intervalley-coherent (K-IVC) state, which spontaneously breaks both \mathcal{T} and $U_v(1)$ symmetry (valley charge conservation), but preserves a ‘Kramers’ time-reversal symmetry represented by $\tau_y\mathcal{K}$, where τ represents Pauli matrices in valley space and \mathcal{K} denotes complex conjugation. Such an emergent symmetry protects the Kramers-like degeneracy of the intervalley-coherent ordered states in the valley space, and the resulting K-IVC states are topological insulators that exhibit \mathbb{Z}_2 topology. The K-IVC state is characterized by an intriguing alternating current-loop pattern on the atomic length scale, which triples the graphene primitive cell⁴⁴.

A further report⁴¹ is of all-band Hartree–Fock calculations that include the valley, spin and sublattice degrees of freedom, and studies of possible ground states at different integer fillings both with and without hBN alignment. The results indicate that the states that spontaneously break flavour symmetry, that is, the valley- and/or spin-polarized states, are energetically favoured at $\pm 1/2$ and $\pm 3/4$ fillings, and would lead to diverse phenomena at different fillings. It was proposed⁴¹ that if the non-interacting Hamiltonian preserves C_{2z} symmetry (that is, a system without hBN alignment), the experimentally observed correlated insulating states at $\pm 1/2$ filling^{17,47} are a nematic valley-polarized state, which spontaneously breaks C_{2z} , \mathcal{T} and C_{3z} symmetries, but preserves the combined symmetry $C_{2z}\mathcal{T}$ (REF.⁴¹). The valley polarization is associated with compensating current loops with antiferromagnetic orbital moments in the moiré supercell (FIG. 5a)⁴¹, which result from the diamagnetic currents of Dirac fermions coupled with the opposite pseudo-magnetic fields, as discussed in the section on topological properties of moiré graphene systems. It has also been proposed⁴¹ that by virtue of the C_{2z} symmetry breaking, the valley-polarized states would exhibit nonlinear optical responses induced by the compensating current-loop order.

Another report¹³³ is of Hartree–Fock calculations with Coulomb interactions projected onto the flat bands, under the assumption that the valley charge is conserved. With such approximations, it was proposed that the ground state at the CNP is a nematic semimetal driven by small heterostrain¹³³.

In REF.⁷⁶, interactions were projected onto the flat bands, and unrestricted Hartree–Fock calculations that included the valley and spin degrees of freedom were performed. The ground states are intervalley-coherent states that spontaneously break $U_v(1)$ symmetry at $\pm 1/4$ filling, $\pm 1/2$ filling and the CNP, but are valley- and spin-polarized states at $\pm 3/4$ filling. This ground state at the CNP reported in REF.⁷⁶ is consistent with those reported in REF.⁴⁴. It is worth noting that, with similar choice of interaction parameters to those used in REF.⁷⁶ (screening length 40 nm and dielectric constant 7) but including effects of nonlocal exchange interactions, the ground state at the CNP reported in REF.⁴¹ is an IVC state, but one that preserves time-reversal symmetry.

In REF.⁷⁷, Hartree–Fock calculations are reported for the flat bands in the hybrid Wannier basis, in which the basis functions are exponentially localized in one direction and remain extended in the orthogonal direction. In this approach, a QAH state with $C = \mp 1$ emerges at ± 3 fillings for intermediate and strong interaction strengths, which can be further stabilized by a staggered

sublattice potential. Another paper¹⁴⁰ reports extensive numerical studies in the basis of hybrid Wannier functions at $1/2$ filling for a spinless one-valley TBG continuum model without hBN alignment. Using both DMRG and variational methods, three competing states for the single-flavour continuum model at $1/2$ filling were identified: a gapped QAH state, a gapless nematic state preserving $C_{2z}\mathcal{T}$ symmetry, and a gapped, $C_{2z}\mathcal{T}$ -preserving and cell-doubling stripe state originating from the gapless nematic state. Such a study is helpful in understanding the nature of the ground state at $3/4$ filling for TBG without hBN alignment^{47,69}.

To better understand the nature of the correlated insulators, theoretical approaches beyond the Hartree–Fock approximations are needed. Because the energy scale of the Coulomb interactions U is typically greater than the bandwidth W (for instance, in magic-angle TBG, $U \approx 25$ meV, $W \approx 10$ meV), it is helpful to consider the strong-coupling limit^{130,141} with $U \gg W$. The strong-coupling approaches are either based on exponentially localized Wannier functions constructed for the four spin-degenerate flat bands from the two valleys^{80,123,130,141,148}, or based on Coulomb interactions projected onto the Bloch eigenstates of the flat bands^{145,149–151}. With certain approximations, the projected Coulomb interactions exhibits symmetries that allow for exact solutions at certain fillings^{130,149}. In particular, REF.¹³⁰ reports an approximate

Glossary

Berry phases

The Berry phase of a Bloch eigenstate is a gauge-invariant phase angle accumulated after an adiabatic and cyclic evolution of the Bloch state in a vector parameter space, which can be the Brillouin zone in a crystalline solid.

Chern numbers

In topological band theory, the Chern number C of an energy band in a 2D crystalline solid is defined as the integration of the Berry curvature over the Brillouin zone.

Density matrix renormalization group

A numerical variational technique devised to solve for the Hamiltonians of low-dimensional quantum many-body systems based on efficient truncations of the many-body Hilbert space.

Filling

The filling factor p is defined as the number of electrons or holes per moiré supercell divided by the fourfold spin-valley degeneracy. p is positive/negative for electron/hole filling with respect to charge neutrality.

Hubbard model

A simple model of interacting particles in a lattice, with only two terms in the Hamiltonian: a kinetic term allowing for hopping of particles between sites of the

lattice, and a potential term consisting of an on-site interaction.

Landau levels

(LL). The quantized energy levels of a 2D electron gas subject to strong perpendicular magnetic fields.

Superconducting domes

A dome-shaped superconducting region that appears in the phase diagrams of many unconventional superconductors such as cuprate superconductors and iron-based superconductors.

Superfluid weight

Non-zero superfluid weight (D_J) is a defining property of superconductors and leads to the Meissner effect and dissipationless transport. It can be more rigorously defined as the change in the free energy density \mathcal{F} due to the motion of Cooper pairs with uniform momentum p_x : $\mathcal{F} = D_J p_x^2 / 8$.

Van Hove singularities

A singularity (non-smooth point) in the density of states of a crystalline solid.

Weyl nodes

In band theory, a twofold band degeneracy point at an arbitrary point in the Brillouin zone of a 3D crystalline solid.

expression for the Coulomb interaction in the Wannier-function basis, which preserves SU(4) symmetry. In this approach, the ground state at 1/2 filling should be an intervalley-coherent state favoured by a second-order perturbation process of the kinetic energy¹³⁰. Another approach is quantum Monte Carlo calculations. Such calculations for the Hamiltonian proposed in REF.¹³⁰ suggest the IVC state and quantum valley Hall state as two candidates for the correlated insulator at the CNP¹³⁹. Moreover, REFS¹⁵⁰ and¹⁴⁹ report a $U(4) \times U(4)$ symmetry from the two valleys for the Coulomb interactions projected onto the exactly flat bands in the chiral limit. The $U(4) \times U(4)$ symmetry is reduced to a $U(4)$ symmetry when the chiral symmetry is absent, and further reduced to $U(2) \times U(2)$ symmetry in a realistic situation that includes kinetic energy (as discussed in the section on moiré lattice structure and symmetries)¹⁵⁰. Treating the kinetic term as a perturbation to the Coulomb-interaction term, it has been argued that the ground states at 0 and $\pm 1/2$ fillings are intervalley-coherent states with zero Chern numbers, whereas the ground states at 1/4 and 3/4 fillings are (partially) valley-polarized states with Chern number ± 1 (REF.¹⁴⁹). These results are partly supported by exact-diagonalization calculations¹⁴⁵.

The various theoretical works suggest that there are multiple competing orders in TBG by virtue of the various degrees of freedom in the system, and the actual ground states in a realistic situation may be sensitive to details such as strain^{133,152}, (weak) external fields and other perturbation terms that are not included in the continuum Hamiltonian. More theoretical and experimental work is needed to unveil the rich properties of TBG.

The close analogy between the flat bands and the zeroth pseudo-LLs make magic-angle TBG a candidate system in which to realize fractional Chern insulator states¹⁰¹. In particular, a Laughlin-like wavefunction on the periodic moiré superlattice for the fractionally filled flat bands in magic-angle TBG in the chiral limit has been constructed¹⁰¹. Numerical calculations that use exact diagonalization for valley-polarized flat Chern bands based on the realistic continuum model for hBN-aligned TBG have identified fractional Chern insulator states at 2/3 (REFS^{153,154}) and 3/5 (REF.¹⁵³) hole fillings with respect to the fully occupied moiré flat bands. These works suggest that the magic-angle TBG, and other moiré graphene systems with topologically non-trivial flat bands^{28,35},

are candidates to study the exotic fractional QAH effect.

Outlook

By virtue of the interplay between strong Coulomb correlations and non-trivial band topology, more intriguing phenomena are expected to emerge in moiré graphene systems and other moiré 2D van der Waals systems. For example, superconductivity shows up in different moiré graphene systems^{16,37}, but its mechanisms are still under debate^{42,125,128,155–160}. Orbital magnetism and the close analogy between the flat bands and pseudo-LLs in TBG may provide a new perspective in understanding the superconductivity in moiré graphene systems¹⁶⁰.

The moiré orbital magnetic states are completely new states of matter. Our understanding of various physical properties of the moiré orbital magnetic states — such as the response to external electric and magnetic fields^{161,162}, collective excitations^{75,151,163,164} and the quantum and classical critical properties — are still at an early stage.

Moreover, some other moiré 2D van der Waals systems such as twisted bilayer–monolayer graphene systems^{38,78,79}, mirror-symmetric twisted trilayer graphene^{58,165–167} and moiré transition metal dichalcogenide systems^{168–178} have been successfully synthesized. A plethora of intriguing phenomena such as correlated density wave states and insulating states^{78,79,172–174,179}, QAH and orbital ferromagnetic states³⁸, superconductors^{165,166,172,175}, unconventional moiré excitons^{168–171} and the nonlinear Hall effect^{180,181} have been observed in these systems. We expect more exciting new physics to emerge in this rapidly developing field of moiré 2D van der Waals materials.

Jianpeng Liu^{1,2} and Xi Dai^{1,2}✉

¹School of Physical Science and Technology, ShanghaiTech University, Shanghai, China.

²ShanghaiTech Laboratory for Topological Physics, ShanghaiTech University, Shanghai, China.

³Department of Physics, Hong Kong University of Science and Technology, Kowloon, Hong Kong, China.

✉e-mail: liujp@shanghaitech.edu.cn; daix@ust.hk

<https://doi.org/10.1038/s42254-021-00297-3>

Published online 13 April 2021

- Varma, C. M. Non-Fermi-liquid states and pairing instability of a general model of copper oxide metals. *Phys. Rev. B* **55**, 14554–14580 (1997).
- Sarma, S. D. & Pinczuk, A. *Perspectives in Quantum Hall Effects: Novel Quantum Liquids in Low-dimensional Semiconductor Structures* (Wiley, 2008).
- Klitzing, K. V., Dorda, G. & Pepper, M. New method for high-accuracy determination of the fine-structure constant based on quantized Hall resistance. *Phys. Rev. Lett.* **45**, 494–497 (1980).

- Thouless, D. J., Kohmoto, M., Nightingale, M. P. & den Nijs, M. Quantized Hall conductance in a two-dimensional periodic potential. *Phys. Rev. Lett.* **49**, 405–408 (1982).
- Tsui, D. C., Stormer, H. L. & Gossard, A. C. Two-dimensional magnetotransport in the extreme quantum limit. *Phys. Rev. Lett.* **48**, 1559 (1982).
- Laughlin, R. B. Anomalous quantum Hall effect: an incompressible quantum fluid with fractionally charged excitations. *Phys. Rev. Lett.* **50**, 1395–1398 (1983).
- Neupert, T., Santos, L., Chamon, C. & Mudry, C. Fractional quantum Hall states at zero magnetic field. *Phys. Rev. Lett.* **106**, 236804 (2011).
- Tang, E., Mei, J.-W. & Wen, X.-G. High-temperature fractional quantum Hall states. *Phys. Rev. Lett.* **106**, 236802 (2011).
- Sun, K., Gu, Z., Katsura, H. & Das Sarma, S. Nearly flatbands with nontrivial topology. *Phys. Rev. Lett.* **106**, 236803 (2011).
- Bistritzer, R. & MacDonald, A. H. Moiré bands in twisted double-layer graphene. *Proc. Natl Acad. Sci. USA* **108**, 12233–12237 (2011).
- Lopes dos Santos, J. M. B., Peres, N. M. R. & Castro Neto, A. H. Graphene bilayer with a twist: electronic structure. *Phys. Rev. Lett.* **99**, 256802 (2007).
- Mele, E. J. Commensuration and interlayer coherence in twisted bilayer graphene. *Phys. Rev. B* **81**, 161405 (2010).
- Trambly de Laissardière, G., Mayou, D. & Magaud, L. Localization of Dirac electrons in rotated graphene bilayers. *Nano Lett.* **10**, 804–808 (2010).
- Lopes dos Santos, J. M. B., Peres, N. M. R. & Castro Neto, A. H. Continuum model of the twisted graphene bilayer. *Phys. Rev. B* **86**, 155449 (2012).
- San-Jose, P., González, J. & Guinea, F. Non-Abelian gauge potentials in graphene bilayers. *Phys. Rev. Lett.* **108**, 216802 (2012).
- Cao, Y. et al. Unconventional superconductivity in magic-angle graphene superlattices. *Nature* **556**, 43–50 (2018).
- Cao, Y. et al. Correlated insulator behaviour at half-filling in magic-angle graphene superlattices. *Nature* **556**, 80–84 (2018).
- Yankowitz, M. et al. Tuning superconductivity in twisted bilayer graphene. *Science* **363**, 1059–1064 (2019).
- Song, Z. et al. All magic angles in twisted bilayer graphene are topological. *Phys. Rev. Lett.* **123**, 036401 (2019).
- Ahn, J., Park, S. & Yang, B.-J. Failure of Nielsen–Ninomiya theorem and fragile topology in two-dimensional systems with space-time inversion symmetry: application to twisted bilayer graphene at magic angle. *Phys. Rev. X* **9**, 021013 (2019).
- Po, H. C., Zou, L., Senthil, T. & Vishwanath, A. Faithful tight-binding models and fragile topology of magic-angle bilayer graphene. *Phys. Rev. B* **99**, 195455 (2019).
- Liu, J., Liu, J. & Dai, X. Pseudo Landau level representation of twisted bilayer graphene: band topology and implications on the correlated insulating phase. *Phys. Rev. B* **99**, 155415 (2019).
- Tarnopolsky, G., Kruchkov, A. J. & Vishwanath, A. Origin of magic angles in twisted bilayer graphene. *Phys. Rev. Lett.* **122**, 106405 (2019).
- Sharpe, A. L. et al. Emergent ferromagnetism near three-quarters filling in twisted bilayer graphene. *Science* **365**, 605–608 (2019).
- Serlin, M. et al. Intrinsic quantized anomalous Hall effect in a moiré heterostructure. *Science* **367**, 900–903 (2020).
- Stepanov, P. et al. Untying the insulating and superconducting orders in magic-angle graphene. *Nature* **583**, 375–378 (2020).
- Zhang, Y.-H., Mao, D., Cao, Y., Jarillo-Herrero, P. & Senthil, T. Nearly flat Chern bands in moiré superlattices. *Phys. Rev. B* **99**, 075127 (2019).
- Liu, J., Ma, Z., Gao, J. & Dai, X. Quantum valley Hall effect, orbital magnetism, and anomalous Hall effect in twisted multilayer graphene systems. *Phys. Rev. X* **9**, 031021 (2019).
- Lee, J. Y. et al. Theory of correlated insulating behaviour and spin-triplet superconductivity in twisted double bilayer graphene. *Nat. Commun.* **10**, 5333 (2019).
- Chebrolov, N. R., Chittari, B. L. & Jung, J. Flat bands in twisted double bilayer graphene. *Phys. Rev. B* **99**, 235417 (2019).
- Cea, T., Walet, N. R. & Guinea, F. Twists and the electronic structure of graphitic materials. *Nano Lett.* **19**, 8683–8689 (2019).

32. Koshino, M. Band structure and topological properties of twisted double bilayer graphene. *Phys. Rev. B* **99**, 235406 (2019).
33. Ma, Z. et al. Topological flat bands in twisted trilayer graphene. *Sci. Bull.* **66**, 18–22 (2020).
34. Haddadi, F., Wu, Q., Kruchkov, A. J. & Yazyev, O. V. Moiré flat bands in twisted double bilayer graphene. *Nano Lett.* **20**, 2410–2415 (2020).
35. Zhang, Y.-H. & Senthil, T. Bridging Hubbard model physics and quantum Hall physics in trilayer graphene/h-BN moiré superlattice. *Phys. Rev. B* **99**, 205150 (2019).
36. Chittari, B. L., Chen, G., Zhang, Y., Wang, F. & Jung, J. Gate-tunable topological flat bands in trilayer graphene boron-nitride moiré superlattices. *Phys. Rev. Lett.* **122**, 016401 (2019).
37. Chen, G. et al. Signatures of tunable superconductivity in a trilayer graphene moiré superlattice. *Nature* **572**, 215–219 (2019).
38. Polshyn, H. et al. Electrical switching of magnetic order in an orbital Chern insulator. *Nature* **588**, 66–70 (2020).
39. Wong, D. et al. Cascade of electronic transitions in magic-angle twisted bilayer graphene. *Nature* **582**, 198–202 (2020).
40. Zondiner, U. et al. Cascade of phase transitions and Dirac revivals in magic-angle graphene. *Nature* **582**, 203–208 (2020).
41. Liu, J. & Dai, X. Theories for the correlated insulating states and quantum anomalous Hall effect phenomena in twisted bilayer graphene. *Phys. Rev. B* **103**, 035427 (2021).
42. Po, H. C., Zou, L., Vishwanath, A. & Senthil, T. Origin of Mott insulating behavior and superconductivity in twisted bilayer graphene. *Phys. Rev. X* **8**, 031089 (2018).
43. Angeli, M., Tosatti, E. & Fabrizio, M. Valley Jahn–Teller effect in twisted bilayer graphene. *Phys. Rev. X* **9**, 041010 (2019).
44. Bultinck, N. et al. Ground state and hidden symmetry of magic-angle graphene at even integer filling. *Phys. Rev. X* **10**, 031034 (2020).
45. Bultinck, N., Chatterjee, S. & Zaletel, M. P. Mechanism for anomalous Hall ferromagnetism in twisted bilayer graphene. *Phys. Rev. Lett.* **124**, 166601 (2020).
46. Zhang, Y.-H., Mao, D. & Senthil, T. Twisted bilayer graphene aligned with hexagonal boron nitride: an anomalous Hall effect and a lattice model. *Phys. Rev. Res.* **1**, 033126 (2019).
47. Lu, X. et al. Superconductors, orbital magnets and correlated states in magic-angle bilayer graphene. *Nature* **574**, 653–657 (2019).
48. Saito, Y., Ge, J., Watanabe, K., Taniguchi, T. & Young, A. F. Independent superconductors and correlated insulators in twisted bilayer graphene. *Nat. Phys.* **16**, 926–930 (2020).
49. Xie, Y. et al. Spectroscopic signatures of many-body correlations in magic-angle twisted bilayer graphene. *Nature* **572**, 101–105 (2019).
50. Jiang, Y. et al. Charge order and broken rotational symmetry in magic-angle twisted bilayer graphene. *Nature* **573**, 91–95 (2019).
51. Kerelsky, A. et al. Maximized electron interactions at the magic angle in twisted bilayer graphene. *Nature* **572**, 95 (2019).
52. Choi, Y. et al. Electronic correlations in twisted bilayer graphene near the magic angle. *Nat. Phys.* **15**, 1174–1180 (2019).
53. Uchida, K., Furuya, S., Iwata, J.-I. & Oshiyama, A. Atomic corrugation and electron localization due to moiré patterns in twisted bilayer graphenes. *Phys. Rev. B* **90**, 155451 (2014).
54. Lee, J.-K. et al. The growth of AA graphite on (111) diamond. *J. Chem. Phys.* **129**, 234709 (2008).
55. Mora, C., Regnault, N. & Bernevig, B. A. Flatbands and perfect metal in trilayer moiré graphene. *Phys. Rev. Lett.* **123**, 026402 (2019).
56. Zhu, Z., Carr, S., Massatt, D., Luskin, M. & Kaxiras, E. Twisted trilayer graphene: a precisely tunable platform for correlated electrons. *Phys. Rev. Lett.* **125**, 116404 (2020).
57. Khalaf, E., Kruchkov, A. J., Tarnopolsky, G. & Vishwanath, A. Magic angle hierarchy in twisted graphene multilayers. *Phys. Rev. B* **100**, 085109 (2019).
58. Lei, C., Linhart, L., Qin, W., Libisch, F. & MacDonald, A. H. Mirror symmetry breaking and stacking-shift dependence in twisted trilayer graphene. Preprint at <https://arxiv.org/abs/2010.05787> (2020).
59. Wu, F., Zhang, R.-X. & Das Sarma, S. Three-dimensional topological twistronics. *Phys. Rev. Res.* **2**, 022010 (2020).
60. Tsai, K.-T. et al. Correlated superconducting and insulating states in twisted trilayer graphene moiré of moiré superlattices. Preprint at <https://arxiv.org/abs/1912.03375> (2019).
61. Jung, J., Raoux, A., Qiao, Z. & MacDonald, A. H. Ab initio theory of moiré superlattice bands in layered two-dimensional materials. *Phys. Rev. B* **89**, 205414 (2014).
62. Moon, P. & Koshino, M. Electronic properties of graphene/hexagonal-boron-nitride moiré superlattice. *Phys. Rev. B* **90**, 155406 (2014).
63. Moon, P. & Koshino, M. Optical absorption in twisted bilayer graphene. *Phys. Rev. B* **87**, 205404 (2013).
64. Ohta, T. et al. Evidence for interlayer coupling and moiré periodic potentials in twisted bilayer graphene. *Phys. Rev. Lett.* **109**, 186807 (2012).
65. Luican, A. et al. Single-layer behavior and its breakdown in twisted graphene layers. *Phys. Rev. Lett.* **106**, 126802 (2011).
66. Li, G. et al. Observation of Van Hove singularities in twisted graphene layers. *Nat. Phys.* **6**, 109–113 (2010).
67. Yan, W. et al. Angle-dependent Van Hove singularities in a slightly twisted graphene bilayer. *Phys. Rev. Lett.* **109**, 126801 (2012).
68. Angeli, M. et al. Emergent D_2 symmetry in fully relaxed magic-angle twisted bilayer graphene. *Phys. Rev. B* **98**, 235137 (2018).
69. Wu, S., Zhang, Z., Watanabe, K., Taniguchi, T. & Andrei, E. Y. Chern insulators, Van Hove singularities and topological flat bands in magic-angle twisted bilayer graphene. *Nat. Mater.* <https://doi.org/10.1038/s41563-020-00911-2> (2021).
70. Das, I. et al. Symmetry broken Chern insulators and magic series of Rashba-like Landau level crossings in magic angle bilayer graphene. *Nat. Phys.* <https://doi.org/10.1038/s41567-021-01186-3> (2021).
71. Nuckolls, K. P. et al. Strongly correlated Chern insulators in magic-angle twisted bilayer graphene. *Nature* **588**, 610–615 (2020).
72. Cao, Y. et al. Tunable correlated states and spin-polarized phases in twisted bilayer–bilayer graphene. *Nature* **583**, 215–220 (2020).
73. Shen, C. et al. Correlated states in twisted double bilayer graphene. *Nat. Phys.* **16**, 520–525 (2020).
74. Liu, X. et al. Tunable spin-polarized correlated states in twisted double bilayer graphene. *Nature* **583**, 221–225 (2020).
75. Wu, F. & Das Sarma, S. Collective excitations of quantum anomalous Hall ferromagnets in twisted bilayer graphene. *Phys. Rev. Lett.* **124**, 046403 (2020).
76. Zhang, Y., Jiang, K., Wang, Z. & Zhang, F. Correlated insulating phases of twisted bilayer graphene at commensurate filling fractions: a Hartree–Fock study. *Phys. Rev. B* **102**, 035136 (2020).
77. Hejazi, K., Chen, X. & Balents, L. Hybrid Wannier Chern bands in magic angle twisted bilayer graphene and the quantized anomalous Hall effect. Preprint at <https://arxiv.org/abs/2007.00134> (2020).
78. Chen, S. et al. Electrically tunable correlated and topological states in twisted monolayer–bilayer graphene. *Nat. Phys.* <https://doi.org/10.1038/s41567-020-01062-6> (2020).
79. Shi, Y. et al. Tunable Van Hove singularities and correlated states in twisted trilayer graphene. Preprint at <https://arxiv.org/abs/2004.12414> (2020).
80. Koshino, M. et al. Maximally localized Wannier orbitals and the extended Hubbard model for twisted bilayer graphene. *Phys. Rev. X* **8**, 031087 (2018).
81. Jung, J., Raoux, A., Qiao, Z. & MacDonald, A. H. Ab initio theory of moiré superlattice bands in layered two-dimensional materials. *Phys. Rev. B* **89**, 205414 (2014).
82. Moon, P. & Koshino, M. Electronic properties of graphene/hexagonal-boron-nitride moiré superlattice. *Phys. Rev. B* **90**, 155406 (2014).
83. Hejazi, K., Liu, C., Shapourian, H., Chen, X. & Balents, L. Multiple topological transitions in twisted bilayer graphene near the first magic angle. *Phys. Rev. B* **99**, 035111 (2019).
84. Nam, N. N. T. & Koshino, M. Lattice relaxation and energy band modulation in twisted bilayer graphene. *Phys. Rev. B* **96**, 075311 (2017).
85. Fang, S. & Kaxiras, E. Electronic structure theory of weakly interacting bilayers. *Phys. Rev. B* **93**, 235153 (2016).
86. Lucignano, P., Alfè, D., Cataudella, V., Ninno, D. & Cantele, G. Crucial role of atomic corrugation on the flat bands and energy gaps of twisted bilayer graphene at the magic angle $\theta \sim 1.08^\circ$. *Phys. Rev. B* **99**, 195419 (2019).
87. Yu, R., Qi, X. L., Bernevig, A., Fang, Z. & Dai, X. Equivalent expression of z_2 topological invariant for band insulators using the non-Abelian Berry connection. *Phys. Rev. B* **84**, 075119 (2011).
88. Soluyanov, A. A. & Vanderbilt, D. Smooth gauge for topological insulators. *Phys. Rev. B* **85**, 115415 (2012).
89. Taherinejad, M., Garrity, K. F. & Vanderbilt, D. Wannier center sheets in topological insulators. *Phys. Rev. B* **89**, 115102 (2014).
90. Haldane, F. D. M. Model for a quantum Hall effect without Landau levels: condensed-matter realization of the ‘parity anomaly’. *Phys. Rev. Lett.* **61**, 2015–2018 (1988).
91. Kane, C. L. & Mele, E. J. Z_2 topological order and the quantum spin Hall effect. *Phys. Rev. Lett.* **95**, 146802 (2005).
92. Kane, C. L. & Mele, E. J. Quantum spin Hall effect in graphene. *Phys. Rev. Lett.* **95**, 226801 (2005).
93. Bernevig, B. A., Hughes, T. L. & Zhang, S. C. Quantum spin Hall effect and topological phase transition in HgTe quantum wells. *Science* **314**, 1757–1761 (2006).
94. Fu, L. & Kane, C. L. Topological insulators with inversion symmetry. *Phys. Rev. B* **76**, 045302 (2007).
95. Po, H. C., Watanabe, H. & Vishwanath, A. Fragile topology and Wannier obstructions. *Phys. Rev. Lett.* **121**, 126402 (2018).
96. Song, Z.-D., Elcoro, L., Xu, Y.-F., Regnault, N. & Bernevig, B. A. Fragile phases as affine monoids: classification and material examples. *Phys. Rev. X* **10**, 031001 (2020).
97. Castro Neto, A. H., Guinea, F., Peres, N. M. R., Novoselov, K. S. & Geim, A. K. The electronic properties of graphene. *Rev. Mod. Phys.* **81**, 109–162 (2009).
98. Uchida, K., Furuya, S., Iwata, J.-I. & Oshiyama, A. Atomic corrugation and electron localization due to moiré patterns in twisted bilayer graphenes. *Phys. Rev. B* **90**, 155451 (2014).
99. Rademaker, L. & Mellado, P. Charge-transfer insulation in twisted bilayer graphene. *Phys. Rev. B* **98**, 235158 (2018).
100. Haldane, F. D. M. & Rezayi, E. H. Periodic Laughlin–Jastrow wave functions for the fractional quantized Hall effect. *Phys. Rev. B* **31**, 2529–2531 (1985).
101. Ledwith, P. J., Tarnopolsky, G., Khalaf, E. & Vishwanath, A. Fractional Chern insulator states in twisted bilayer graphene: an analytical approach. *Phys. Rev. Res.* **2**, 023237 (2020).
102. Hofstadter, D. R. Energy levels and wave functions of Bloch electrons in rational and irrational magnetic fields. *Phys. Rev. B* **14**, 2239–2249 (1976).
103. Lian, B., Xie, F. & Bernevig, B. A. Landau level of fragile topology. *Phys. Rev. B* **102**, 041402 (2020).
104. Peotta, S. & Törmä, P. Superfluidity in topologically nontrivial flat bands. *Nat. Commun.* **6**, 8944 (2015).
105. Hu, X., Hyart, T., Pikulin, D. I. & Rossi, E. Geometric and conventional contribution to the superfluid weight in twisted bilayer graphene. *Phys. Rev. Lett.* **123**, 237002 (2019).
106. Julku, A., Peltonen, T. J., Liang, L., Heikkilä, T. T. & Törmä, P. Superfluid weight and Berezinskii–Kosterlitz–Thouless transition temperature of twisted bilayer graphene. *Phys. Rev. B* **101**, 060505 (2020).
107. Xie, F., Song, Z., Lian, B. & Bernevig, B. A. Topology-bounded superfluid weight in twisted bilayer graphene. *Phys. Rev. Lett.* **124**, 167002 (2020).
108. Chen, G. et al. Tunable correlated Chern insulator and ferromagnetism in a moiré superlattice. *Nature* **579**, 56–61 (2020).
109. Zhu, J., Su, J.-J. & MacDonald, A. H. Voltage-controlled magnetic reversal in orbital Chern insulators. *Phys. Rev. Lett.* **125**, 227702 (2020).
110. Tschirhart, C. et al. Imaging orbital ferromagnetism in a moiré Chern insulator. Preprint at <https://arxiv.org/abs/2006.08053> (2020).
111. Li, S.-Y. et al. Experimental evidence for orbital magnetic moments generated by moiré-scale current loops in twisted bilayer graphene. *Phys. Rev. B* **102**, 121406 (2020).
112. Ceresoli, D., Thonhauser, T., Vanderbilt, D. & Resta, R. Orbital magnetization in crystalline solids: multi-band insulators, Chern insulators, and metals. *Phys. Rev. B* **74**, 024408 (2006).
113. Macdonald, A. H. Introduction to the physics of the quantum Hall regime. Preprint at <https://arxiv.org/abs/cond-mat/9410047> (1994).
114. Nagaosa, N., Sinova, J., Onoda, S., MacDonald, A. & Ong, N. Anomalous Hall effect. *Rev. Mod. Phys.* **82**, 1539 (2010).

115. Liu, J. & Dai, X. Anomalous Hall effect, magneto-optical properties, and nonlinear optical properties of twisted graphene systems. *npj Comput. Mater.* **6**, 57 (2020).
116. He, W.-Y., Goldhaber-Gordon, D. & Law, K. T. Giant orbital magnetoelectric effect and current-induced magnetization switching in twisted bilayer graphene. *Nat. Commun.* **11**, 1650 (2020).
117. Su, Y. & Lin, S.-Z. Current-induced reversal of anomalous Hall conductance in twisted bilayer graphene. *Phys. Rev. Lett.* **125**, 226401 (2020).
118. Huang, C., Wei, N. & MacDonald, A. Current driven magnetization reversal in orbital Chern insulators. *Phys. Rev. Lett.* **126**, 056801 (2021).
119. Ying, X., Ye, M. & Balents, L. Current switching of valley polarization in twisted bilayer graphene. Preprint at <https://arxiv.org/abs/2101.01790> (2021).
120. Kraut, W. & von Baltz, R. Anomalous bulk photovoltaic effect in ferroelectrics: a quadratic response theory. *Phys. Rev. B* **19**, 1548–1554 (1979).
121. Sipe, J. E. & Shkrebtii, A. I. Second-order optical response in semiconductors. *Phys. Rev. B* **61**, 5337–5352 (2000).
122. Gao, Y., Zhang, Y. & Xiao, D. Tunable layer circular photogalvanic effect in twisted bilayers. *Phys. Rev. Lett.* **124**, 077401 (2020).
123. Kang, J. & Vafeek, O. Symmetry, maximally localized Wannier states, and a low-energy model for twisted bilayer graphene narrow bands. *Phys. Rev. X* **8**, 031088 (2018).
124. Yuan, N. F. Q. & Fu, L. Model for the metal–insulator transition in graphene superlattices and beyond. *Phys. Rev. B* **98**, 045103 (2018).
125. Isobe, H., Yuan, N. F. Q. & Fu, L. Unconventional superconductivity and density waves in twisted bilayer graphene. *Phys. Rev. X* **8**, 041041 (2018).
126. Xu, X. Y., Law, K. T. & Lee, P. A. Kekulé valence bond order in an extended Hubbard model on the honeycomb lattice with possible applications to twisted bilayer graphene. *Phys. Rev. B* **98**, 121406 (2018).
127. Huang, T., Zhang, L. & Ma, T. Antiferromagnetically ordered Mott insulator and $d + d$ superconductivity in twisted bilayer graphene: a quantum Monte Carlo study. *Sci. Bull.* **64**, 310–314 (2019).
128. Liu, C.-C., Zhang, L.-D., Chen, W.-Q. & Yang, F. Chiral spin density wave and $d + d$ superconductivity in the magic-angle-twisted bilayer graphene. *Phys. Rev. Lett.* **121**, 217001 (2018).
129. Venderbos, J. W. F. & Fernandes, R. M. Correlations and electronic order in a two-orbital honeycomb lattice model for twisted bilayer graphene. *Phys. Rev. B* **98**, 245103 (2018).
130. Kang, J. & Vafeek, O. Strong coupling phases of partially filled twisted bilayer graphene narrow bands. *Phys. Rev. Lett.* **122**, 246401 (2019).
131. Xie, M. & MacDonald, A. H. Nature of the correlated insulator states in twisted bilayer graphene. *Phys. Rev. Lett.* **124**, 097601 (2020).
132. Jian, C.-M. & Xu, C. Moire Mott insulators viewed as the surface of three dimensional symmetry protected topological phases. Preprint at <https://arxiv.org/abs/1810.03610> (2018).
133. Liu, S., Khalaf, E., Lee, J. Y. & Vishwanath, A. Nematic topological semimetal and insulator in magic-angle bilayer graphene at charge neutrality. *Phys. Rev. Res.* **3**, 013033 (2021).
134. Chatterjee, S., Bultinck, N. & Zaletel, M. P. Symmetry breaking and skyrmionic transport in twisted bilayer graphene. *Phys. Rev. B* **101**, 165141 (2020).
135. Alavirad, Y. & Sau, J. Ferromagnetism and its stability from the one-magnon spectrum in twisted bilayer graphene. *Phys. Rev. B* **102**, 235123 (2020).
136. Repellin, C., Dong, Z., Zhang, Y.-H. & Senthil, T. Ferromagnetism in narrow bands of moiré superlattices. *Phys. Rev. Lett.* **124**, 187601 (2020).
137. Angeli, M., Tosatti, E. & Fabrizio, M. Valley Jahn–Teller effect in twisted bilayer graphene. *Phys. Rev. X* **9**, 041010 (2019).
138. Lu, C. et al. Chiral so (4) spin-charge density wave and degenerate topological superconductivity in magic-angle-twisted bilayer-graphene. Preprint at <https://arxiv.org/abs/2003.09513> (2020).
139. Da Liao, Y. et al. Correlation-induced insulating topological phases at charge neutrality in twisted bilayer graphene. *Phys. Rev. X* **11**, 011014 (2021).
140. Kang, J. & Vafeek, O. Non-Abelian Dirac node braiding and near-degeneracy of correlated phases at odd integer filling in magic-angle twisted bilayer graphene. *Phys. Rev. B* **102**, 035161 (2020).
141. Seo, K., Kotov, V. N. & Uchoa, B. Ferromagnetic Mott state in twisted graphene bilayers at the magic angle. *Phys. Rev. Lett.* **122**, 246402 (2019).
142. Yuan, N. F., Isobe, H. & Fu, L. Magic of high-order Van Hove singularity. *Nat. Commun.* **10**, 5769 (2019).
143. Chichinadze, D. V., Classen, L. & Chubukov, A. V. Valley magnetism, nematicity, and density wave orders in twisted bilayer graphene. *Phys. Rev. B* **102**, 125120 (2020).
144. Soejima, T., Parker, D. E., Bultinck, N., Hauschild, J. & Zaletel, M. P. Efficient simulation of moiré materials using the density matrix renormalization group. *Phys. Rev. B* **102**, 205111 (2020).
145. Xie, F. et al. TBG VI: an exact diagonalization study of twisted bilayer graphene at non-zero integer fillings. Preprint at <https://arxiv.org/abs/2010.00588> (2020).
146. Saito, Y. et al. Hofstadter subband ferromagnetism and symmetry-broken Chern insulators in twisted bilayer graphene. *Nat. Phys.* <https://doi.org/10.1038/s41567-020-01129-4> (2021).
147. Park, J. M., Cao, Y., Watanabe, K., Taniguchi, T. & Jarillo-Herrero, P. Flavour Hund's coupling, correlated Chern gaps, and diffusivity in moiré flat bands. Preprint at <https://arxiv.org/abs/2008.12296> (2020).
148. Chen, B.-B. et al. Realization of topological Mott insulator in a twisted bilayer graphene lattice model. Preprint at <https://arxiv.org/abs/2011.07602> (2020).
149. Lian, B. et al. TBG IV: exact insulator ground states and phase diagram of twisted bilayer graphene. Preprint at <https://arxiv.org/abs/2009.13530> (2020).
150. Bernevig, B. A., Song, Z., Regnault, N. & Lian, B. TBG III: interacting Hamiltonian and exact symmetries of twisted bilayer graphene. Preprint at <https://arxiv.org/abs/2009.12376> (2020).
151. Bernevig, B. A. et al. TBG V: exact analytic many-body excitations in twisted bilayer graphene Coulomb Hamiltonians: charge gap, goldstone modes and absence of Cooper pairing. Preprint at <https://arxiv.org/abs/2009.14200> (2020).
152. Parker, D. E., Soejima, T., Hauschild, J., Zaletel, M. P. & Bultinck, N. Strain-induced quantum phase transitions in magic angle graphene. Preprint at <https://arxiv.org/abs/2012.09885> (2020).
153. Repellin, C. & Senthil, T. Chern bands of twisted bilayer graphene: fractional Chern insulators and spin phase transition. *Phys. Rev. Research* **2**, 023238 (2020).
154. Abouelkomsan, A., Liu, Z. & Bergholtz, E. J. Particle-hole duality, emergent Fermi liquids, and fractional Chern insulators in moiré flatbands. *Phys. Rev. Lett.* **124**, 106803 (2020).
155. Xu, C. & Balents, L. Topological superconductivity in twisted multilayer graphene. *Phys. Rev. Lett.* **121**, 087001 (2018).
156. Wu, F., MacDonald, A. H. & Martin, I. Theory of phonon-mediated superconductivity in twisted bilayer graphene. *Phys. Rev. Lett.* **121**, 257001 (2018).
157. Lian, B., Wang, Z. & Bernevig, B. A. Twisted bilayer graphene: a phonon-driven superconductor. *Phys. Rev. Lett.* **122**, 257002 (2019).
158. Wu, F. Topological chiral superconductivity with spontaneous vortices and supercurrent in twisted bilayer graphene. *Phys. Rev. B* **99**, 195114 (2019).
159. Hsu, Y.-T., Wu, F. & Das Sarma, S. Topological superconductivity, ferromagnetism, and valley-polarized phases in moiré systems: renormalization group analysis for twisted double bilayer graphene. *Phys. Rev. B* **102**, 085103 (2020).
160. Khalaf, E., Chatterjee, S., Bultinck, N., Zaletel, M. P. & Vishwanath, A. Charged skyrmions and topological origin of superconductivity in magic angle graphene. Preprint at <https://arxiv.org/abs/2004.00638> (2020).
161. Herzog-Arbeitman, J., Song, Z.-D., Regnault, N. & Bernevig, B. A. Hofstadter topology: non-crystalline topological materials in the moiré era. *Phys. Rev. Lett.* **125**, 236804 (2020).
162. Wu, Q., Liu, J., Guan, Y. & Yazyev, O. V. Landau levels as a probe for band topology in graphene moiré superlattices. *Phys. Rev. Lett.* **126**, 056401 (2021).
163. Khalaf, E., Bultinck, N., Vishwanath, A. & Zaletel, M. P. Soft modes in magic angle twisted bilayer graphene. Preprint at <https://arxiv.org/abs/2009.14827> (2020).
164. Vafeek, O. & Kang, J. Renormalization group study of hidden symmetry in twisted bilayer graphene with Coulomb interactions. *Phys. Rev. Lett.* **125**, 257602 (2020).
165. Park, J. M., Cao, Y., Watanabe, K., Taniguchi, T. & Jarillo-Herrero, P. Tunable strongly coupled superconductivity in magic-angle twisted trilayer graphene. *Nature* **590**, 249–255 (2021).
166. Hao, Z. et al. Electric field tunable superconductivity in alternating twist magic-angle trilayer graphene. *Science* <https://doi.org/10.1126/science.abg0399> (2021).
167. Li, X., Wu, F. & MacDonald, A. H. Electronic structure of single-twist trilayer graphene. Preprint at <https://arxiv.org/abs/1907.12338> (2019).
168. Tran, K. et al. Evidence for moiré excitons in van der Waals heterostructures. *Nature* **567**, 71–75 (2019).
169. Seyler, K. L. et al. Signatures of moiré-trapped valley excitons in MoSe₂/WSe₂ heterobilayers. *Nature* **567**, 66–70 (2019).
170. Jin, C. et al. Observation of moiré excitons in WSe₂/WS₂ heterostructure superlattices. *Nature* **567**, 76–80 (2019).
171. Alexeev, E. M. et al. Resonantly hybridized excitons in moiré superlattices in van der Waals heterostructures. *Nature* **567**, 81–86 (2019).
172. Wang, L. et al. Correlated electronic phases in twisted bilayer transition metal dichalcogenides. *Nat. Mater.* **19**, 861–866 (2020).
173. Regan, E. C. et al. Mott and generalized Wigner crystal states in WSe₂/WS₂ moiré superlattices. *Nature* **579**, 359–363 (2020).
174. Tang, Y. et al. Simulation of Hubbard model physics in WSe₂/WS₂ moiré superlattices. *Nature* **579**, 353–358 (2020).
175. An, L. et al. Interaction effects and superconductivity signatures in twisted double-bilayer WSe₂. *Nanoscale Horiz.* **5**, 1309–1316 (2020).
176. Li, H. et al. Imaging moiré flat bands in 3D reconstructed WSe₂/WS₂ superlattices. Preprint at <https://arxiv.org/abs/2007.06113> (2020).
177. Jin, C. et al. Stripe phases in WSe₂/WS₂ moiré superlattices. Preprint at <https://arxiv.org/abs/2007.12068> (2020).
178. Xu, Y. et al. Correlated insulating states at fractional fillings of moiré superlattices. *Nature* **587**, 214–218 (2020).
179. Rickhaus, P. et al. Density-wave states in twisted double-bilayer graphene. Preprint at <https://arxiv.org/abs/2005.05373> (2020).
180. Huang, M. et al. Giant nonlinear Hall effect in twisted WSe₂. Preprint at <https://arxiv.org/abs/2006.05615> (2020).
181. Hu, J.-X., Zhang, C.-P., Xie, Y.-M. & Law, K. T. Nonlinear Hall effects in strained twisted bilayer WSe₂. Preprint at <https://arxiv.org/abs/2004.14140> (2020).

Acknowledgements

J.L. acknowledges a start-up grant from ShanghaiTech University and the National Key R&D programme of China (Grant No. 2020YFA0309601). X.D. acknowledges financial support from the Hong Kong Research Grants Council (Project No. GRF16300918 and No. 16309020).

Author contributions

The authors contributed equally to all aspects of the article.

Competing interests

The authors declare no competing interests.

Peer review information

Nature Reviews Physics thanks the anonymous reviewers for their contribution to the peer review of this work.

Publisher's note

Springer Nature remains neutral with regard to jurisdictional claims in published maps and institutional affiliations.

© Springer Nature Limited 2021